Brittle origin of off-fault fractures during the 2019 Ridgecrest earthquake sequence

Enrico Milanese, Camilla Cattania

Department of Earth, Atmospheric, and Planetary Sciences, Massachusetts Institute of Technology, Cambridge, MA, USA

SUMMARY

According to the classical Mohr-Coulomb-Anderson theory, faults form at an angle from the largest regional compressive stress that is approximately 30° for most rocks. However, real settings are more complex and faults often present orientations inconsistent with the angles predicted by the classical theory applied to the present-day regional stress field. The Ridgecrest region hosts a young fault system that is part of the Eastern California Shear Zone, and the 2019 earthquake sequence unveiled orthogonal ruptures at multiple scales, apparently at odds with the classical brittle failure model. We use the Ridgecrest region as a case study and compare surface ruptures that developed during the 2019 earthquake sequence to the expected orientations derived from classical faulting theory and to observations from rock experiments. We focus on the off-fault secondary fractures that developed coseismically at the northern termination of the mainshock fault. We calculate coseismic stress changes from published slip models superimposed to a background stress field. We find that a combination of tectonic regional stresses oriented with the largest compressive stress at N14E and weak intensity of coseismic stresses best captures the orientation of off-fault fractures in the classical Mohr-Coulomb-Anderson framework, with an internal rock friction coefficient $\mu = 0.6$. The secondary fractures also show a scale separation: long fractures are best compatible with shear failure, while short frac-with either local normal faulting or early tensile failures that would later coalesce to form longer faults, consistent with growth of shear fractures in laboratory experiments. Finally, the different orientations of fractures that developed during and prior to the 2019 events suggest that the tectonic stress has rotated over geological timescales. When accounting for the specificity of the area, orthogonal faulting is thus compatible with brittle fracturing with typical experimental values of rock friction coefficient.

Key words: Dynamics and mechanics of faulting – Fractures, faults, and high strain deformation zones – Fault zone rheology – Earthquake dynamics – North America

1 INTRODUCTION

Upon stress release, tectonic loading can result in both formation of new faults and earthquakes or other slip events along pre-existing faults. In young fault systems, both phenomena are observed and are often widespread in the faulting region (e.g. in the Eastern California Shear Zone (ECSZ), Dokka & Travis (1990)), while mature systems release most of the energy in the form of slip along a set of faults and by accumulating damage in their close proximity. The region of Ridgecrest that hosted the 2019 earthquake sequence is part of the ECSZ and it is an appropriate case study to investigate fault formation because of its young age and of the large amount of ruptures that surfaced during the 2019 sequence.

Faulting is most often described with the classical Mohr-Coulomb-Anderson theory as the development of a shear plane in the crust due to the local stress field. The theory is inspired and supported by experimental evidence that rocks, when subject to multi-axial compression, develop fractures that coalesce along a slipping plane. Assuming a Coulomb failure criterion, the angle θ_μ that this plane forms from the largest compressive stress σ_1 is determined as $\theta_\mu = \left(\pi/2 - \tan^{-1}\mu\right)/2$, where μ is the rock internal friction coefficient. The value of μ can vary with the loading conditions but it is most commonly found between 0.6 and 1.0 (although values up to 1.5 have been reported (Anderson 1951; Paterson & Wong 2005; Jaeger et al. 2009)), implying θ_μ =23–30°. Because of the symmetry of the magnitude of the shear stresses acting on two planes at opposite angles from σ_1, two conjugate failure planes can develop at $\pm\theta_\mu$, and second-order effects determine which of the two prevails at sample-size failure. The two planes differ for the orientation of the shear stresses and, thus, of the slip. Combining Mohr-Coulomb theory with rock multi-axial experiments, one would expect faults to form at θ_μ =23–30° from the local σ_1, and indeed this is often observed (e.g. Anderson (1951); Nixon et al. (2011)). However, several fault systems exhibit different angles, for example orthogonal conjugate faults, i.e. θ_μ =45–50° (Thatcher & Hill 1991; Liang et al. 2021; Scholz & Choi 2022), in contradiction with the typical values of μ. This would imply a coefficient of friction near zero, or, in other words, that the host rock has negligible shear resistance.

Orthogonal faulting is common in the ECSZ (Thatcher & Hill 1991), and the region of Ridgecrest that hosted the 2019 sequence is of particular interest, as it displays conjugate faults at unfavorable orientations at all scales (Ross et al. 2019; Antoine et al. 2021; Fialko & Jin 2021). The 2019 earthquake sequence is characterized by two main events – the July 4 M_w 6.4 foreshock and the July 5 M_w 7.1 mainshock – that ruptured two conjugate faults that are approximately orthogonal and that were not previously extensively mapped (Thompson Jobe et al. 2020). Both shocks were followed by intense seismic activity and several off-fault fractures developed coseismically (Ross et al. 2019; DuRoss et al. 2020; Thompson Jobe et al. 2020; Ponti et al. 2020; Xu et al. 2020b; Antoine et al. 2021; Rodriguez Padilla et al. 2022). If one assumes a uniform and time-independent stress field, the orthogonality of both the main faults and of the off-fault fractures requires a near-zero coefficient of friction. Alternatively, other factors could be at play: the stress field could be heterogeneous due to historical and recent earthquakes, and ancient faults may not reflect the present day stress field.

Here, we test the hypothesis that theory and observations are actually reconciled when one considers the stress state due to both the tectonic loading and the coseismic stress release, and variations in the tectonic stress orientation over geological timescales. We estimate expected fracture orientation in the total stress field, accounting for regional and coseismic stresses, for a range of plausible regional stress orientations, coseismic stress drops, and coefficients of friction. Our analysis shows a length-scale separation where long fractures are compatible with shear failure with $\mu = 0.6$–1.0 and short ones with normal faulting or tensile failure, commonly observed before linkage into fully developed shear fractures in laboratory experiments. Finally, we put our results in the context of the geological history of the region, showing that the orthogonality between the dextral mainshock fault and the several sinistral coseismic surface ruptures and aftershock faults can be ascribed to a long-term rotation of the tectonic stress state and their different temporal origins.

2 METHODS

2.1 Available data

Fig. 1a shows the Ridgecrest region in Southern California, and the surface ruptures recorded by Ponti et al. (2020) following the July 2019 earthquake sequence. The surface ruptures were obtained with different methodologies: mapped directly on the field, derived from digital surface models, obtained from satellite-based radar or optical imagery, and inferred from later compilation of field observations (Ponti et al. 2020). The M_w 6.4 foreshock ruptured a SW-NE trending strand, and the M_w 7.1 mainshock the longer SE-NW trending strand. Two main mechanically unfavorable features appear from the surface ruptures: the two orthogonal conjugate faults activated by the foreshock and mainshock, and several smaller-scale ruptures in the North-West that developed at high angles ($\approx 90°$) with respect to the mainshock fault (dashed rectangle in Fig. 1a and 1b).

In the following we focus on the NW off-fault features; Ross et al. (2019), Fialko & Jin (2021), Liang et al. (2021) and Scholz & Choi (2022) have investigated the orthogonality of the mainshock and foreshock faults. For our analysis we used the dataset of Ponti et al. (2020), removing ruptures that dated prior to 2019, as identified by Thompson Jobe et al. (2020) based on later field verifications and studies of geomorphic maps and geospatial datasets. We investigated both the entire dataset, and a subset of fractures with known slip sense (based on DuRoss et al. (2020); Xu et al. (2020a); Antoine et al. (2021), see Fig. 1b), which place a tighter constraint on the stress field.

2.2 Assumptions and predicted orientations estimation

To estimate the compatibility of Coulomb failure we determine the shear plane orientation at the center of each rupture for a range of values of friction coefficient, regional stress orientation, and intensity of the coseismic stresses. We then identify the combination of parameters that best fits the observed fracture orientation and discuss their significance.

To estimate the shear plane orientation, i.e. the predicted fracture orientation, we proceed as follows. Assuming an Andersonian regime, the occurrence of strike-slip events implies a horizontal σ_1 in the total stress field (given by the superposition of regional and coseismic stress), with shear failure planes oriented at $\theta_\text{s} = \theta_\text{H}(x_\text{s}, y_\text{s}) \pm \theta_\mu$, where $\theta_\text{H}(x_\text{s}, y_\text{s})$ is the orientation of the largest horizontal compressive stress $\sigma_\text{H}(x_\text{s}, y_\text{s})$ at the center of the rupture segment s. We use this estimate for fractures with horizontal slip, chosing the plane consistent with observed slip direction. On the other hand, normal faulting indicates an extensional regime with vertical σ_1, and fault strike parallel to the maximum horizontal stress ($\sigma_H = \sigma_2$), so that $\theta_\text{s}(\sigma_H) = \theta_H$. We use this expression for dip-slip fractures. Note that this is the same orientation expected for tensile cracks if σ_1 was horizontal ($\sigma_H = \sigma_1$), and some ambiguity exists if the slip or opening direction is not reported. The tectonic stress field in the Ridgecrest region is close to transtensional: $\sigma_1 \approx \sigma_2 = 3\sigma_3$ (Fialko 2021), with regional stress components $\sigma_\text{H,reg} = \sigma_1$, $\sigma_\text{v,reg} = \sigma_2$, $\sigma_\text{h,reg} = \sigma_3$, and we further assume the regional stresses to be lithostatic (e.g., at 100 m depth is $\sigma_1 = \sigma_2 = 1.67$ MPa and $\sigma_3 = 0.56$ MPa, see Supplementary Text). We weight coseismic stress changes computed at 100 m depth by a factor k ($0 \leq k \leq 1$). This allows us to look at two possible interpretations: i) as the cosesimic stresses intensity is not reached instantly during the earthquake, k represents at what level of intensity the fractures formed; ii) as the regional stresses

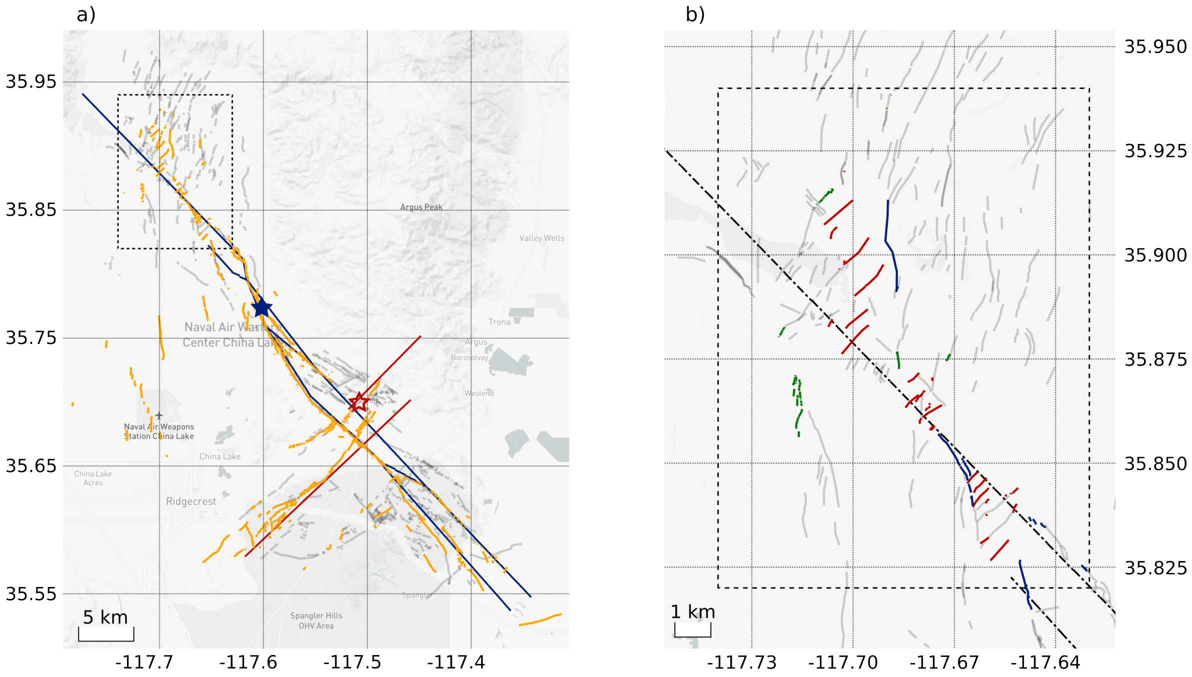

Figure 1. Surface ruptures in the Ridgecrest region and investigated area. a) Surface ruptures (orange lines) due to the 2019 Ridgecrest sequence in Southern California, US, as reported by Ponti et al. (2020). Red and blue stars show the epicenter of the M_w 6.4 foreshock and M_w 7.1 mainshock, respectively; fault traces of the sinistral foreshock and dextral mainshock as modelled by Jin & Fialko (2020) are in red and blue solid line, respectively. b) Subset of surface ruptures of known slip-sense: sinistral (red), dextral (blue), or vertical (green) (DuRoss et al. 2020; Xu et al. 2020a; Antoine et al. 2021); black dash-dotted line identifies fault trace of the mainshock as modelled by Jin & Fialko (2020). In both panels, the dashed rectangle identifies the studied region, and features developed prior to 2019 (Thompson Jobe et al. 2020) are represented in dark grey lines. Features from Ponti et al. (2020) that ruptured also prior to 2019 (Thompson Jobe et al. 2020) are not visualized. Interactive version available at `https://github.com/enrico-mi/Ridgecrest-visualization.git`.

are assumed lithostatic, they increase linearly with depth, and k is also representive of stress states at different depths. $k = 0$ is then equivalent to considering only the regional stresses, and $k \leq 1$ is also representative of total stress states at depths larger than 100 m, where the lithostatic stresses are larger and have more weight in the estimates of θ_{H}.

We estimate θ_{s} for a range of values of μ and of $\theta_{\mathrm{H,reg}}$, the orientation of the largest tectonic horizontal compression $\sigma_{\mathrm{H,reg}}$. We investigated values of $\theta_{\mathrm{H,reg}}$ between N10W and N25E, expanding the range N0E-N15E reported in the literature (Xu et al. (2020b); Fialko & Jin (2021); Hauksson & Jones (2020); Yang & Hauksson (2013); Wang & Zhan (2020); Sheng & Meng (2020); Milliner et al. (2022), see Supplementary Text). When estimating θ_{s}, we tested three possible scenarios for θ_μ: i) spatially constant, with μ in the range $[0, 1.5]$ (shear failure), ii) spatially constant, with $\theta_\mu = 0$ (normal faulting or tensile failure), and iii) μ randomly drawn from the uniform interval $(0, 1)$, different for each fracture's segment. The latter is used to verify that the Anderson-Mohr-Coulomb criterion is a better predictor than randomness. When analyzing the dataset of ruptures with known slip mechanism, the orientation of each segment is compared to the expected orientation, i.e. $\theta_{\mathrm{DS}} = \theta_{\mathrm{H}}$ (dip slip), $\theta_{\mathrm{RL}} = \theta_{\mathrm{H}} - \theta_{\mu}$ (right-lateral), or $\theta_{\mathrm{LL}} = \theta_{\mathrm{H}} + \theta_{\mu}$ (left-lateral). When we include ruptures with unknown slip mechanism, all fractures in the dataset are compared to all the three possible orientations, and the best fit for each is chosen. To determine how each set of parameters (μ, $\theta_{\mathrm{H,reg}}$, coseismic stress intensity k) performs for each considered subset of ruptures, we estimate the sum of residuals $\mathrm{SR_w}$ of the error ϵ_{w} of the predicted orientation θ_{s} of each fracture segment (see Supplementary Text for more details).

2.3 Predicted and observed orientations

We first investigate the effect of the regional stress orientation and the friction coefficient on the prediction of the fracture orientation. We analyze the subset of fractures with known slip sense (Fig. 1a), considering $\theta_{\mathrm{H,reg}}$, and only the regional stresses ($k = 0$, Fig. 2b). We find that the $\theta_{\mathrm{H,reg}}$ at N14E and $\mu = 0.6$ best capture the fractures orientation. These values correspond to the smallest sum of residuals ($\mathrm{SR_{w,min}} = 12.54°$, Fig. 2a), and Fig. 3 shows a map comparing the predicted and observed orientations. $\mathrm{SR_w}$ is within 5% of this value for $\theta_{\mathrm{H,reg}}$ between N10E and N19E, and in this range of $\theta_{\mathrm{H,reg}}$, $\mathrm{SR_w}$ is always minimized by $\mu = 0.6$. The smallest errors at the boundary of the explored range are $\mathrm{SR_w} = 14.93°$ for $\mu = 0.9$ at N25E, and $\mathrm{SR_w} = 22.97°$ for $\mu = 0.0$ at N10W.

To investigate the relative role of coseismic and regional stresses, we assume $\theta_{\mathrm{H,reg}}$ at N14E and we compute the total stresses at 100 m, multiplying the seismic component by a factor k between 0 and 1 (with 0.1 increments). We find the smallest sum of residuals $\mathrm{SR_w}$ ($\mathrm{SR_{w,min}} = 12.42°$) for $\mu = 0.6$ and $k = 0.1$ (Fig. 2b). Accounting for all the coseismic stress ($k = 1$) produces a poor fit, as the lowest error is $\mathrm{SR_w} = 23.98°$ for $\mu = 1.2$. The second best fit is $k = 0$ ($\mathrm{SR_w} = 12.54°$), for $\mu = 0.6$. For $k \geq 0.2$, $\mathrm{SR_w}$ is more than 5% larger than $\mathrm{SR_{w,min}}$, and it increases with k. The maps of Fig. 4 show the predicted and observed failure directions for the different faulting mechanisms and fractures for $\theta_{\mathrm{H,reg}}$ at N14E and $k = 0.1$.

The best fits are consistent with the relative predicted orientations of fractures of different slip mechanisms. Fig. 5 shows the angle between the predicted fracture orientation and the local largest horizontal compressive stress, measured as the weighted median of $\theta_{\mathrm{s}} - \theta_{\mathrm{H}}$ as a function of k and $\theta_{\mathrm{H,reg}}$, and broken down by slip mechanism: right-lateral (blue), dip slip (green), and left-lateral (red). The three mechanisms are expected to be ordered as $\theta_{\mathrm{RL}} < \theta_{\mathrm{DS}} < \theta_{\mathrm{LL}}$, with $2\theta_{\mu} = \theta_{\mathrm{LL}} - \theta_{\mathrm{RL}}$ being the dihedral angle. The order is well captured by the regional stress ($k = 0$, Fig. 5a) and for $k \leq 0.5$ for $\theta_{\mathrm{H,reg}}$ at N14 (Fig. 5b). For $\theta_{\mathrm{H,reg}}$ near N10E we find $\theta_{\mathrm{DS}} = \theta_{\mathrm{H}}$ and θ_{LL} and θ_{RL} approximately symmetric with respect to θ_{H}, as expected (Fig. 6a). When varying k ($\theta_{\mathrm{H,reg}}$ at N14E, Fig. 5b), we

Misfit as a function of the regional stress orientation $\theta_{\mathrm{H,reg}}$

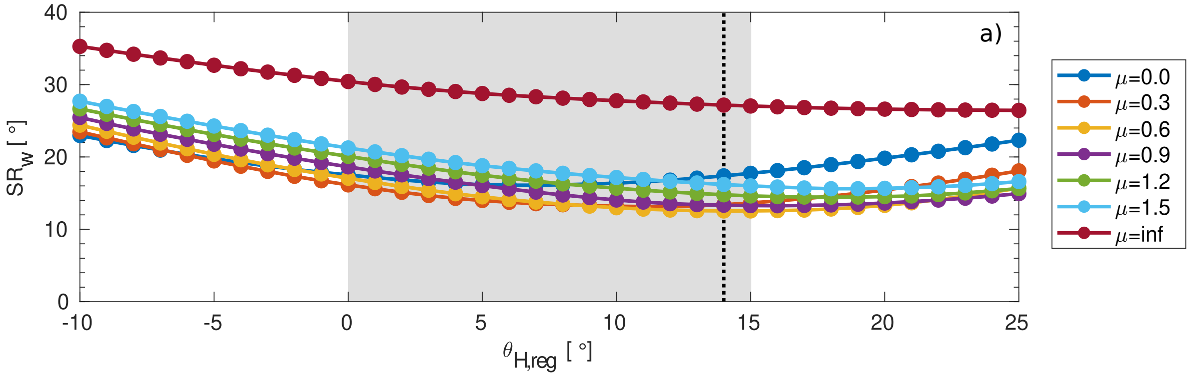

Misfit as a function of the coseismic stresses intensity k

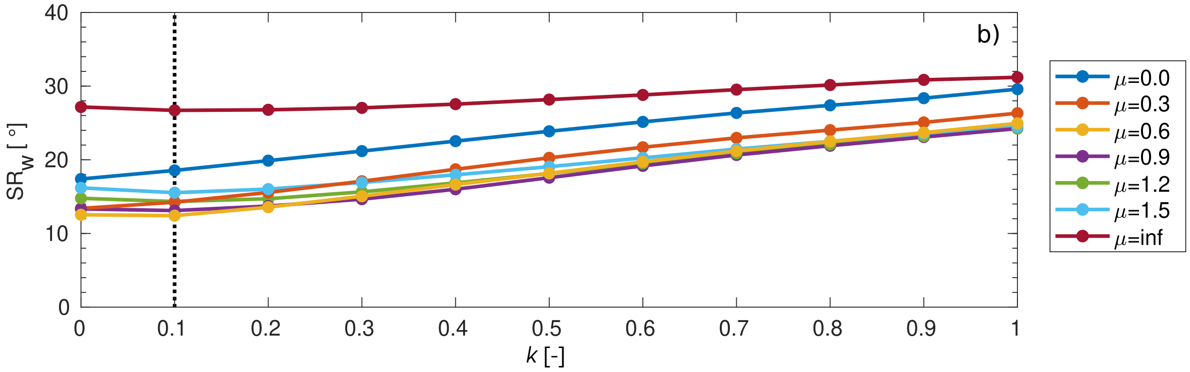

Figure 2. Sum of residuals $\mathrm{SR_w}$ as a function of the regional stress orientation $\theta_{\mathrm{H,reg}}$ (a) and of the coseismic stresses intensity k (b). Solid colored lines identify select values of μ. a) $\mathrm{SR_w}$ is computed for regional stresses only ($k = 0$) at different angles $\theta_{\mathrm{H,reg}}$. $\mathrm{SR_w}$ is minimum at N14E (vertical black dotted line) and $\mu = 0.6$ (yellow marker). Gray shaded area identifies range of values of $\theta_{\mathrm{H,reg}}$ suggested for the region (see Discussion and Methods). b) $\mathrm{SR_w}$ is computed from the total stresses at 100 m depth, regional stresses oriented at N14E. $\mathrm{SR_w}$ is minimum for $k = 0.1$ (vertical black dotted line) and $\mu = 0.6$ (yellow markers), and a comparable value in the absence of coseismic stresses ($k = 0$). For both a) and b), μ values of 0.6 and 0.9 minimize the error; for $k = 0$ also $\mu = 0.3$ gives comparably good fits.

observe that $k \geq 0.7$ implies $\theta_{\mathrm{DS}} > \theta_{\mathrm{LL}}$, which is mechanically incorrect (Fig. 6a). For $k = 0.1$, it is $\theta_{\mathrm{DS}} \approx \theta_{\mathrm{H}}$ and θ_{LL} and θ_{RL} approximately symmetric with respect to θ_{H}, consistently with this parameters' combination being the best fit (Figs 2 and 4).

As the ruptures in the dataset show a wide range of lengths and resolutions (Supplementary Figs S1 and S2), we investigated if μ could depend on the length-scale, assuming $\theta_{\mathrm{H,reg}}$ at N14E. When we consider the subset of fractures of known slip mechanism (Fig. 7), short fractures show predominantly dip slip (Fig. 7b), and longer fractures show both right- and left-lateral shear displacement (Fig. 7c-f). The best fit for fractures shorter and longer than 10 m is $\theta_{\mu} = 0°$ (Supplementary Fig. S3c) and

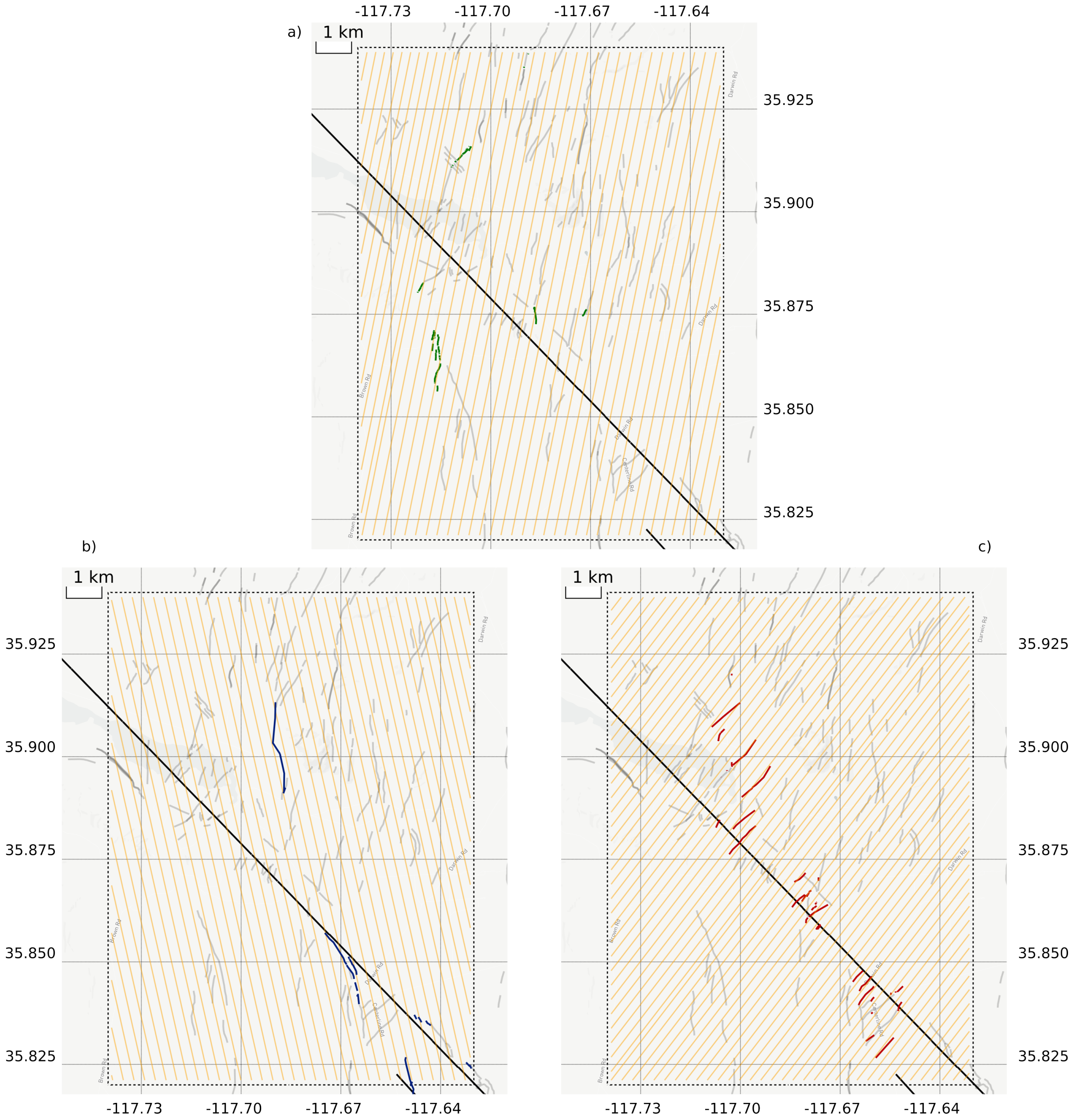

Figure 3. Comparison of fracture orientations and predicted failure planes for fractures of known slip type, $\theta_{\mathrm{H,reg}}$ at N14E, $\mu = 0.6$, and absence of coseismic stresses ($k = 0$). a) Fractures displaying dip slip displacement (green) and direction $\theta_{\mathrm{H,reg}}$ of $\sigma_{\mathrm{H,reg}}$. b) Fractures displaying dextral displacement (blue) and direction of expected dextral failure $\theta_{\mathrm{H,reg}} - \theta_{\mu}$. c) Fractures displaying sinistral displacement (green) and direction of expected sinistral failure $\theta_{\mathrm{H,reg}} + \theta_{\mu}$. Solid black line identifies the fault trace from Jin & Fialko (2020). Grey lines identify ancient features (Thompson Jobe et al. 2020). The classical brittle shear failure criterion well captures the orientation of the many sinistral fractures, which appear orthogonoal to the mainshock fault (c), and of the dextral ruptures (b).

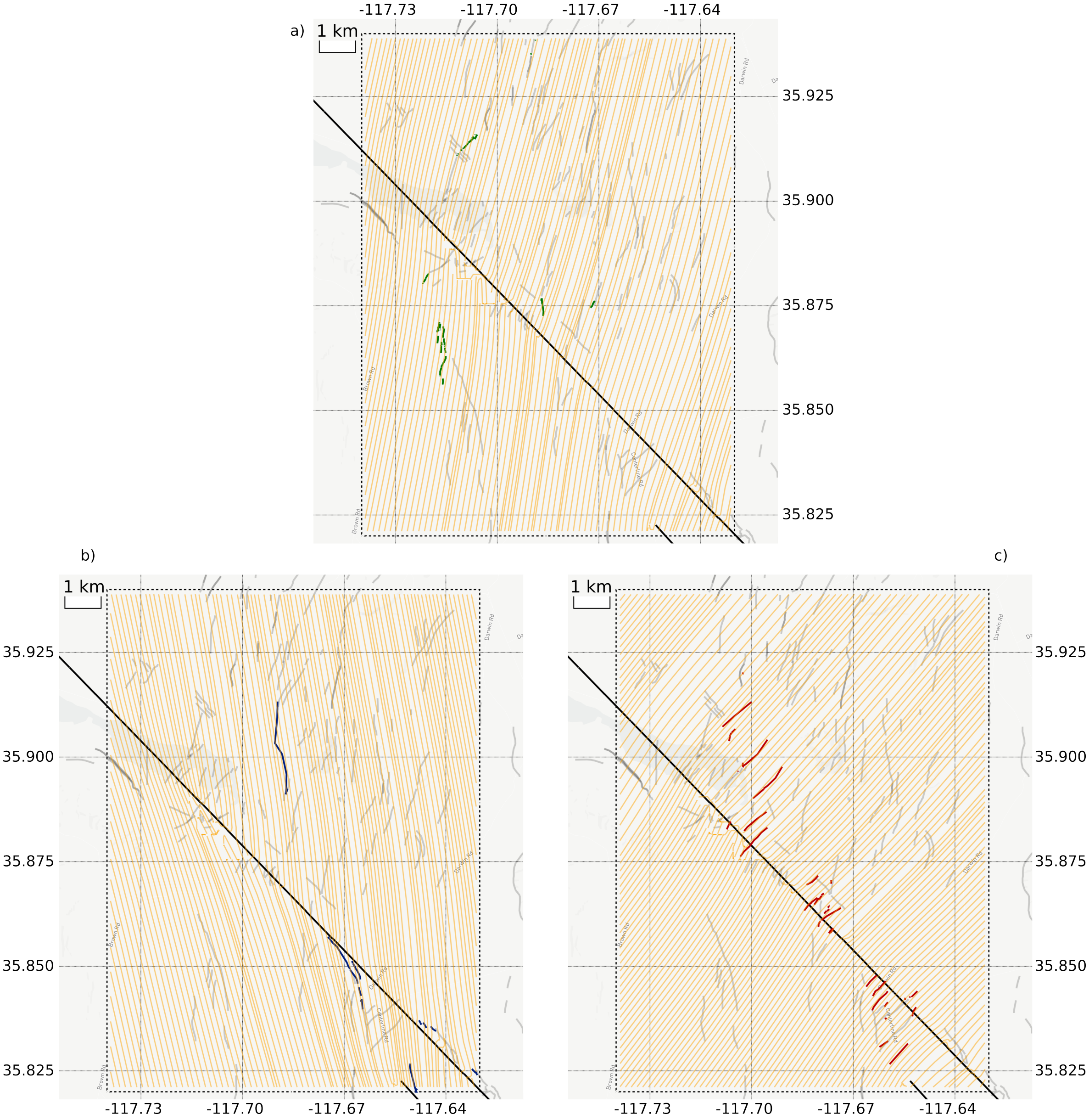

Figure 4. Comparison of fracture orientations and failure planes for fractures of known slip type, $\theta_{\mathrm{H,reg}}$ at N14E, $\mu = 0.6$, and total stresses estimated at 100 m depth and $k = 0.1$. a) Fractures displaying dip slip (green) and direction θ_{H} of σ_{H}. b) Fractures displaying dextral displacement (blue) and direction of expected dextral failure $\theta_{\mathrm{H}} - \theta_{\mu}$. c) Fractures displaying sinistral displacement (green) and direction of expected sinistral failure $\theta_{\mathrm{H}} + \theta_{\mu}$.

$\mu = 0.6$ ($\theta_{\mu} = 29.5°$), respectively. These are consistent with the observed slip mechanisms, as $\mu = 0.6$ is representative of shear failure, and $\theta_{\mu} = 0°$ is expected for fractures parallel to σ_{H}, although it does not provide information on the value of μ (as dip slip is observed, σ_1 is vertical and μ cannot be deduced from the surface plane).

We further expanded this analysis to all the coseismic fractures, including those with unknown

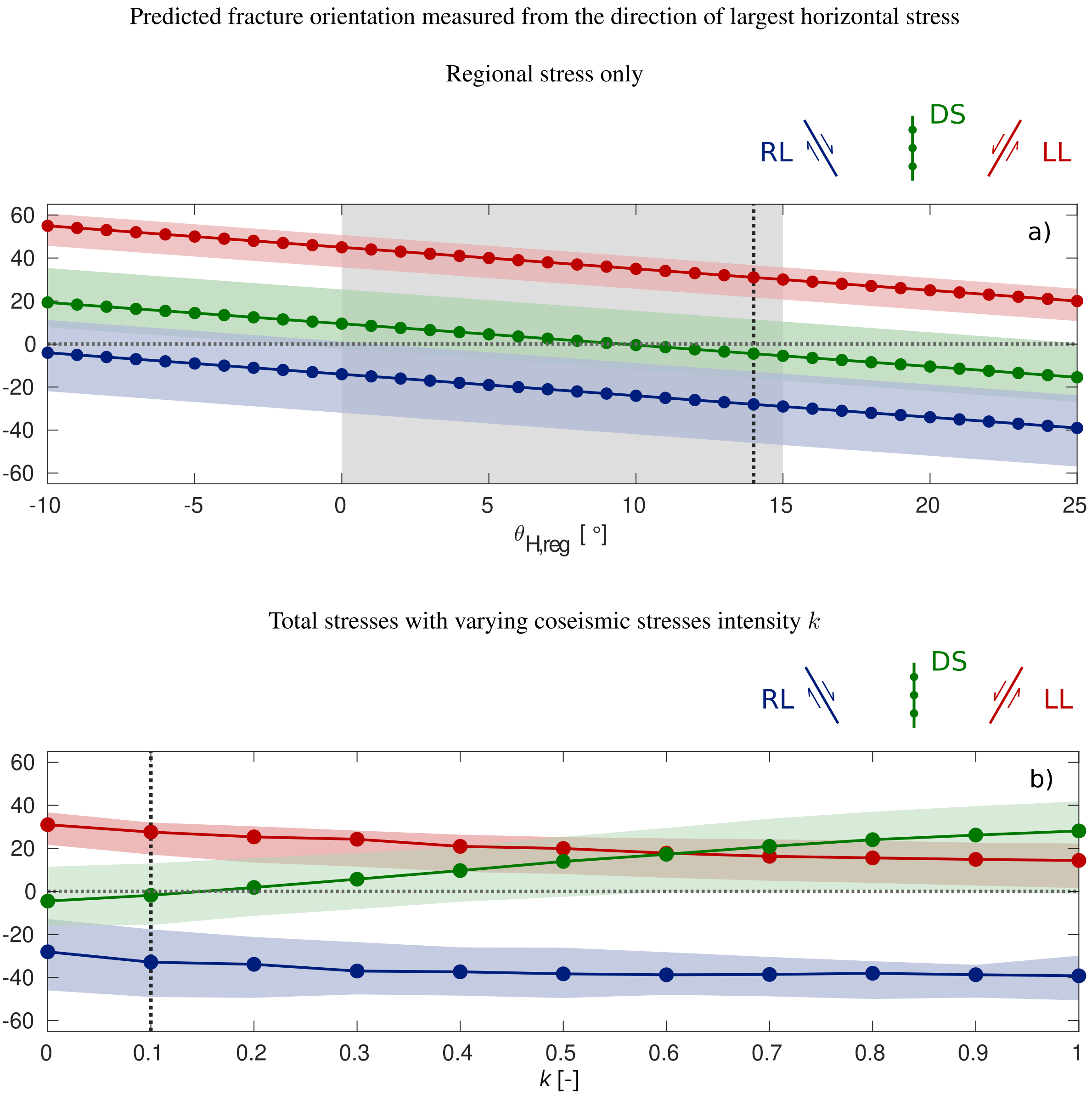

Figure 5. Predicted fracture orientation measured from the direction of largest horizontal stress. The orientation is the weighted median of $\theta_s - \theta_H$ as a function of the regional stress orientation $\theta_{H,reg}$ (a) and of the coseismic stresses intensity k (b). Blue, green, and red represent fractures displaying dextral, dip, and sinistral slip, respectively. Solid lines indicate weighted median, shaded regions identify 25th and 75th percentiles. Vertical black dotted line identifies best fit. Positive (negative) angle values indicate eastward (westward) rotation. a) The best fit for the regional stress only ($k = 0$) is at N14E ($\theta_{H,reg} = 14°$), when horizontal displacements are symmetrical with respect to 0°, and dip slip is close to 0°. The gray shaded area identifies range of values of $\theta_{H,reg}$ suggested for the region (see Discussion and Methods). b) θ_H is computed from the total stresses at 100 m depth, with regional stresses oriented at N14E. When $k = 0.1$, fractures displaying dip slip are centered around 0°, and sinistral and dextral fractures are symmetric around this value (with $\theta_\mu \approx 30°$). This is consistent with the expected relative orientations for brittle shear failure of rocks (see Fig. 6a).

slip sense (orange features within the dotted area in Fig. 1a), still assuming $\theta_{\mathrm{H,reg}}$ at N14E. We also considered the total stress state at depths from 100 m to 500 m (with 100 m increment), with $k = 1$, to link the intensity of the coseismic stresses to a physical dimension: this will later allow us to investigate any correlation with the fractures length. As no information about the slip mechanism is included, the maximum absolute error ϵ_{abs} depends on μ, and $\mathrm{SR_w}$ is therefore normalized by ϵ_{abs} (see Supplementary Text). The best fit for μ for fractures shorter than 10 m is 1.5 ($\theta_\mu = 16.8°$, Supplementary Fig. S3a). $\mu = 1.5$ is the second highest value of μ that we considered in our parametric study, the largest being infinity ($\theta_\mu = 0°$), and a value larger than 1.5 might thus have been a better fit. We interpret this result as an indication that short fractures are oriented at a very low angle from $\theta_{\mathrm{H,reg}}$, suggesting normal faulting or tensile opening, and the value of μ is then not representative of the actual rock friction. When we consider fractures longer than 10 m, the best fit is for $\mu = 1.0$ ($\theta_\mu = 22.5°$, Supplementary Fig. S3b), compatible with shear failure. These fits are consistent with the distribution of strike angles with the fracture length L (Supplementary Fig. S4): short fractures have a wide distribution and cluster around N5E (L <10 m, Fig. S4b), while long fractures show two clusters in the ranges N50W-N0E and N20E-N55E (Supplementary Fig. S4c-f).

3 DISCUSSION

Our results suggest that the orientation of coseismic ruptures is compatible with a brittle Coulomb shear origin with $\mu = 0.6$–1.0 in a stress field governed mostly by the regional tectonic stress with the largest compression axis oriented at N14E.

3.1 Regional stress orientation

The estimated orientation of the largest regional horizontal stress at N14E is consistent with previous estimates in the range N0E-N15E (Xu et al. (2020b); Fialko & Jin (2021); Hauksson & Jones (2020); Yang & Hauksson (2013); Wang & Zhan (2020); Sheng & Meng (2020); Milliner et al. (2022), see also Methods), and our analysis supports the larger values that are observed specifically at the northern end of the mainshock fault. When we consider the lower end of this range ($\theta_{\mathrm{H,reg}}$ at N0E), total stresses at 100 m depth, and k between 0 and 1, the best fit is for $\mu = 0.3$ ($\mathrm{SR_{w,min}} = 14.33$, Supplementary Fig. S5) for fractures of known slip sense. This value of μ is not mechanically compatible as it would imply that the intact host rock has lower resistance to shear fracturing than to frictional sliding, given that the coefficient of sliding friction for the Ridgecrest mainshock fault has been found to be $0.4 < \mu_{\mathrm{s}} \leq 0.75$ from applications of Sibson's criterion for slip onset (Hauksson & Jones 2020; Fialko 2021) and reconstructed stress fields from observed slip distributions (Milliner et al. 2022; Nevitt et al.

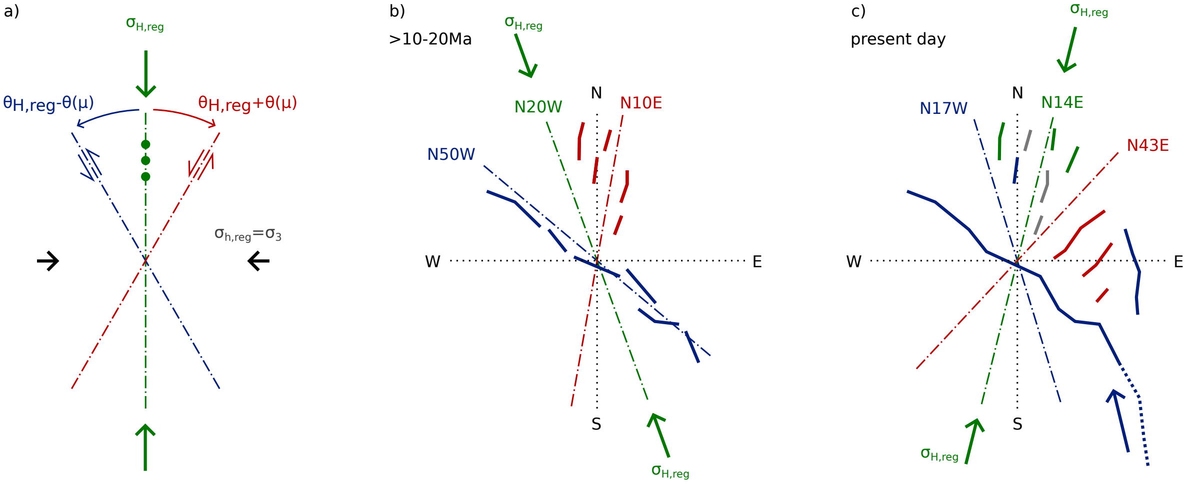

Figure 6. Evolution of tectonic stress and fracture orientation and slip sense. a) Shear failure modes in a transtensional setting: the least compressive horizontal stress coincides with the least compressive principal stress $\sigma_{\text{h,reg}} = \sigma_3$, while the largest compressive horizontal stress is approximately equal to the vertical stress, thus $\sigma_{\text{H,reg}} = \sigma_1 \approx \sigma_2 = \sigma_{\text{v}}$. Conjugate planes appear at $\pm\theta_\mu$ from the axis of principal compression $\theta_{\text{H,reg}}$, with left-lateral (right-lateral) slip for positive (negative) values of θ_μ. Normal faulting can take place at $\theta_{\text{H,reg}}$. Left-lateral, right-lateral, and dip slip motion are depicted in red, blue, and green, respectively. Dash-dotted lines identify directions of compression or slip. b) Ancient faulting more than 10 Ma in a largest compressive regional stress west of north (here assumed at N20W for illustrative purposes). Shear ruptures form on conjugate planes at $2\theta = 60°$ ($\mu = 0.6$), with sinistral faulting aligned at N10E and dextral at N50W. c) Faulting in the present-day stress field, with $\theta_{\text{H,reg}}$ at N14E following a significant rotation of $\sigma_{\text{H,reg}}$. New sinistral (red) and dextral (blue) conjugate faults form in the current stress field (Fig. 1b). N10E-trending faults observed today include both faults originated in the ancient field (b) that are now inactive (gray) or display oblique vertical (green) and dextral (blue) slip, and normal faults formed when the region was an extensional basin after the stress rotation and before the current-day transtensional setting. Dextral faults that formed in the ancient stress field (b) coalesced into the northern termination of the 2019 mainshock fault, that, even if possibly not optimally oriented with respect to the current-day stress field, can still host dextral slip that propagates northward after nucleating in sections of the fault more favorably oriented (blue arrow).

2023). (Note the exception of Xu et al. (2020b), who derive $\mu = 0.1$ to match their slip model and the slip sense of most faults that they observed with radar interferometry.) Our results are consistent in particular with orientations of $\theta_{\text{H,reg}}$ identified by Wang & Zhan (2020), Sheng & Meng (2020), and Milliner et al. (2022), who reported values of N11E, N10.8E±2.8, and N13E±1.8, respectively, for the northern termination of the 2019 mainshock fault. Values closer to N0E are usually identified when the stress orientation is resolved at the scale of the whole Ridgecrest region, not of different fault strands (Xu et al. 2020b; Townend & Zoback 2004; Fialko & Jin 2021; Yang & Hauksson 2013).

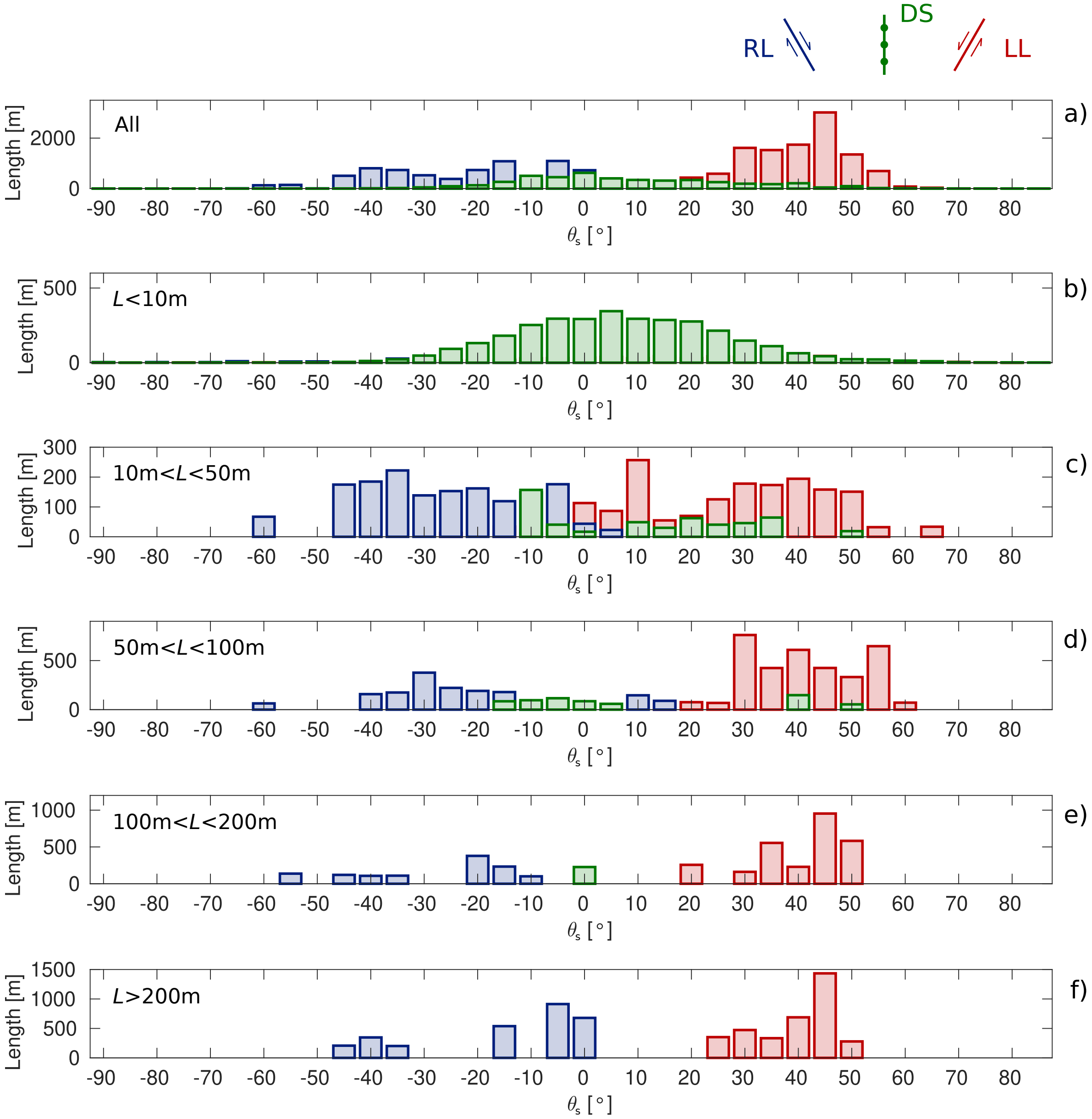

Figure 7. Dependence of fractures strikes on their length L for fractures of known slip sense. Blue, green, and red represent dextral, dip, and sinistral slip, respectively. The whole set (a) shows the separation of the strike distribution by slip mechanism (see also Fig. 1b). Fractures shorter than 10 m (b) cluster around N5E and display dip slip. Longer fractures (c-f) are predominantly right- and left-lateral.

The scenario of the regional stress oriented at N14E dominating the fractures orientation is further supported by the following observations.

First, if one assumes that the depth of a fracture is of the same order of magnitude of its length at the surface, one would expect the orientation of long fractures to be affected largely by the regional stress (assumed lithostatic), which our observations confirm (Supplementary Fig. S6). Under the same assumption, short fractures should be affected mostly by the coseismic stress. However, the distribution of $\theta_s - \theta_H$ for short fractures actually shows a peak at 40° instead of 0 when the coseismic stresses are the largest (Fig. 5b for $k = 1$, and Supplementary Fig. S7), and the regional stress alone or with modest coseismic stresses better captures their orientation (Fig. 5a and Supplementary Fig. S6). As most short fractures that developed during the 2019 sequence display dip slip motion (Figs 1b and 7), they could then be the first stage of damage along planes of normal faulting governed by the regional stress, or en echelon fractures that will later coalesce along shear planes.

Another observation that suggests that regional stresses dominate the orientation of the fractures comes from the aftershock sequence. At the northern termination, the aftershocks that followed the 2019 sequence displayed focal mechanisms with focal planes at N50E (or N40W) down to 11 km deep (Wang & Zhan 2020). Faulting at N50E is compatible with $\theta_{\mathrm{H,reg}}$ at N20E assuming $\mu = 0.6$, hinting at high-angle fractures having formed at all depths, not just at the surface.

3.2 Coseismic stress intensity

Our results indicate that a modest amount of coseismic stresses ($k = 0.1$) best reproduces the observed fracture orientations. Since that the orientation of principal stresses depends on the relative amplitude of background and coseismic stresses, this parameter is closely related to the ratio of coseismic stress drop to half the regional differential stress ($\Delta\tau/\tau$), which is routinely estimated from focal mechanisms (Hardebeck & Okada 2018). Hardebeck & Hauksson (2001) introduced a technique to estimate $\Delta\tau/\tau$ in the near field of a rupture, where the stress tensor can be approximated by its value on the fault plane. For the M$_w$ 7.1 Ridgecrest mainshock, at the northern termination Milliner et al. (2022) found $\Delta\tau/\tau = 0.3$, while Sheng & Meng (2020) report a local rotation of 1.2°, which gives $\Delta\tau/\tau = 0.2$ (applying Eq. 4 in Hardebeck & Hauksson (2001)). We can compare these values for our forward estimates of $\Delta\tau/\tau$, as follows. We approximate $\Delta\tau$ by the shear stress at the center of the fractures, resolved at 45° from the regional σ_1 stresses ($\Delta\tau = 0.45 - 0.62$ MPa). Taking the regional stress at 100m depth ($\tau = 0.56$ MPa), we find $\Delta\tau/\tau = 0.8 - 1.1$. This value is approximately one order of magnitude larger than earlier estimates, largely due to the use of a shallow regional stress field (100 m): we find that the same calculation at a depth of 1km yields $\Delta\tau/\tau = 0.1$, consistent with the values $0.2 - 0.3$ from Milliner et al. (2022) and Sheng & Meng (2020). Our value of $k = 0.1$ for a calculation depth of 100 m corresponds to $\Delta\tau/\tau \approx 0.1$, in agreement with earlier studies, and it could indicate that the fractures are the superficial traces of deeper fractures that surfaced during the sequence. In the latter case, the fracture strikes would be dominated by the most favourable orientation at deeper depths, where $\Delta\tau/\tau$ is lower and compatible with smaller rotations of the principal stresses. Other interpretations are also plausible: (1) fractures formed at the early stages of the earthquake propagation (when $\Delta\tau/\tau$ had not yet reached its final value); (2) our assumption of homogeneous elastic properties leads to an underestimation of the coseismic stress changes, as the shallow crust is possibly more compliant than deeper layers.

Both regional and coseismic stresses are subject to uncertainties. One assumption in the regional stress field that affects k is the ratio $\sigma_{\mathrm{H,reg}}/\sigma_{\mathrm{v,reg}} = 3$. This ratio, estimated by Fialko (2021), is supported by the range of values inferred by Milliner et al. (2022), yet their central values give $\sigma_{\mathrm{H,reg}}/\sigma_{\mathrm{v,reg}} = 2.3$. If the latter is closer to the real regional stress state during fault rupture, the differential stress would be lower than we assumed, requiring even lower values of k to explain the observed rupture orientations. The coseismic stress field is subject to the uncertainties inherent to slip models, i.e. due to the inversion method, the assumed fault geometry and its discretization, the assumed mechanical properties of the rock (e.g. Cattania et al. (2014)). We used the slip model of Jin & Fialko (2020) because of its high spatial resolution (and public availability), in an effort to minimize this source of uncertainty.

The low value of k could indicate that fractures developed during the seismic rupture, before stresses have reached their final value. The crust rock could be already close to failure at the late stages of the seismic cycle, so that a small stress perturbation could be sufficient to cause faulting. This should be further investigated, as we did not model the dynamic propagation of the rupture and its stress field, rather we uniformly applied the coefficient k to the peak coseismic stresses. We also do not rule out dynamic fracturing, as our analysis does not include any dynamic effects, yet the propagation velocities of the foreshock and mainshock were relatively slow. Kinematic models have estimated them between 0.6 and 2.2 km/s (Liu et al. 2019; Goldberg et al. 2020; Wang et al. 2020; Yang et al. 2020; Chen et al. 2020), with an estimate of 1.4 km/s for the mainshock towards the northern termination (Yang et al. 2020). This value is around 40% of the shear wave speed at the hypocenter, and dynamic stresses do not differ much from static ones at these propagation velocities (Freund 1998; Poliakov et al. 2002). A possible scenario is then that damage accumulates under the long action of the regional tectonic stress, and that seismic events eventually rupture planes that were weakened interseismically at lower strain-rates. Seismicity would then affect mostly the timing of the fractures, but less so their orientation. This is consistent with laboratory triaxial experiments, where the sample-wide failure develops on a shear plane at the usual angle θ_μ following acceleration of damage accumulation and coalescence of microcracks that developed quasi-statically and mostly aligned with σ_1 (Renard et al. 2018).

3.3 Values of the internal friction coefficient μ

Experimentally determined values of the internal rock friction coefficient μ are generally in the range 0.6-1.5 (Paterson & Wong 2005), with the larger values being less common. Triaxial tests on samples from the San Andreas Fault Observatory at Depth (SAFOD) are consistent with this range, as Lee & Haimson (2011) report fracture dip angles between 60° and 70° (i.e. $\theta_\mu = 20$–30° and $\mu = 0.6$–1.2). Our results suggest $\mu = 0.6$, consistent with the expected range. This value is also consistent with Byerlee's friction ($\mu_s = 0.6 - 0.8$, with μ_s coefficient of static sliding friction, Byerlee (1978)), which has been suggested for Ridgecrest's mainshock fault (Fialko & Jin 2021; Milliner et al. 2022), has been observed in sliding experiments of SAFOD samples (Tembe et al. 2006; Morrow et al. 2007; Carpenter et al. 2009), and can be assumed as a lower bound for μ. Nonetheless, these values of μ cannot explain orthogonal faulting on their own, unless we remove the assumption that the faults have different temporal origin.

3.4 Faults orthogonality at multiple scales and their temporal origin

Orthogonality of faults has been observed at all scales in the Ridgecrest region, and the implication that fitting for μ based on the Mohr-Coulomb-Anderson theory leads to the unphysical value of $\mu = 0$ has suggested dynamic fracturing (Ross et al. (2019), see Discussion in *Coseismic stress intensity* section), bookshelf kinematics (Antoine et al. 2021; Milliner et al. 2021), or deep ductile failure (Liang et al. 2021; Scholz & Choi 2022) as alternative mechanisms. Ductile failure seems unlikely to apply to the off-fault fractures at the northern termination of the 2019 mainshock fault as this mechanism is usually justified for larger faults (10^1–10^2 km scale) whose interseismic loading is driven by an underlying ductile zone that extends at depth (Scholz & Choi 2022). As for bookshelf kinematics, Milliner et al. (2021) suggested fracture rotations smaller than 0.1°, and it is thus compatible with our observations.

Faulting can also be affected by pre-existing material heterogeneities. In the region, the Independence Dike Swarm (IDS) that formed around 148 Ma might have favored the development of the mainshock fault (Nevitt et al. 2023), yet the IDS NW-orientation is not compatible with the orientation of most fractures object of this study.

The relative temporal origin of the fractures is relevant to the estimates of μ. In particular, when $\mu = 0$ is inferred for sets of orthogonal fractures, it is generally assumed that all formed at the same time and have not rotated since their formation, which is not necessarily the case. Fialko & Jin (2021) showed that the foreshock and mainshock faults likely formed at the same time 5-10 Ma but have rotated away from the axis of largest compression. The same behavior has been suggested for other fault systems in the ECSZ (Ron et al. 2001). In this scenario, Fialko & Jin (2021) suggest that the two faults formed at an angle $2\theta_\mu = 60^\circ$ that later grew by clockwise (counter-clockwise) rotation of the foreshock (mainshock) fault with respect to the largest compression axis, which in turn also rotated clockwise.

Our results are consistent with such a scenario where the mainshock fault formed in an ancient stress field, different from the one the 2019 ruptures surfaced in. The mainshock and foreshock faults formed 5-20 Ma in a stress field with largest horizontal stress oriented west of north (Zoback et al. (1981); Fialko & Jin (2021), and Fig. 6b). Consistently with the ECSZ observed mechanics, the dextral mainshock fault has not rotated significantly, while the sinistral fault has accumulated more rotation and is now orthogonal to the mainshock fault. Over the same arc of time, the tectonic stress field has also rotated, clockwise, to the present day orientation at N14E and until the rotation has been large enough to favor new rock fracturing (Handin 1969; Sibson 1985). The strike of new faults formed in the present-day stress field then appears orthogonal to the older, mainshock fault (Fig. 6c), yet they are compatible with a shear origin with $\mu = 0.6 - 1.0$. This is consistent with the experiments of Handin (1969), where fracturing at 85° from the pre-existing fault plane and slip along such plane concurrently take place when the stress state has rotated away from the condition of favoring slip.

To put our analysis in perspective with the tectonic history of the region we also investigated the orientations of tectonic features prior to the 2019 sequence (Thompson Jobe et al. 2020). In the area we are considering, these features cluster at an angle that well aligns with the present-day tectonic regional stress, without showing any scale separation (Supplementary Fig. S8). These fractures are then compatible with normal faulting ($\theta_s \approx \theta_{\mathrm{H,reg}}$) in the present-day stress field, consistently with the ruptures that hosted dip slip during the 2019 sequence (Figs 1b and 7). This history of dip slip is consistent with the transtensional nature of the stress state in the Ridgecrest region. As $\sigma_{\mathrm{H}} = \sigma_1 \approx \sigma_2 = \sigma_{\mathrm{v}}$, small reductions in σ_{H} are sufficient to change the faulting type from strike-slip to dip-slip. Most of the ancient fractures and of the 2019 dip-slip ruptures are in the tensile quadrant of the mainshock fault, where a coseismic reduction of σ_{H} and change of faulting mechanism to dip-slip is expected (Supplementary Fig. S9). At the same time, σ_{H} was probably oriented between N5W and N30W 10-20 Ma (Zoback et al. 1981; Ron et al. 2001; Fialko & Jin 2021), and ancient features might have thus first developed under strike-slip faulting, favourably oriented in the ancient stress orientation. This would also explain ancient features oriented at N50W, and the formation of Ridgecrest NW-SE trending fault that hosted the mainshock in 2019 (Fig. 6).

We further observe that a cluster of ruptures displaying dip slip is localized in the compressional quadrant (approximately at $[-117.72, 35.86]$, Fig. 1b). This is unexpected, as coseismic stresses in this area should reduce $\sigma_2 = \sigma_{\mathrm{v}}$ and favour strike-slip faulting (Fig. S9). These ruptures though are in close proximity of a previously mapped strand of the Airport Lake fault zone, a Quaternary fault system with a similar orientation. The area might then have accumulated damage and weak planes that favour reactivation along the observed direction with a dip-slip mechanism.

4 CONCLUSIONS

We have investigated the mechanical origins of the high-angle fractures that surfaced at the northern termination of the Ridgecrest mainshock fault during the 2019 earthquake sequence, and put our results in the perspective of the tectonic history of the region.

The high-angle fractures encountered at the northern termination of the mainshock fault are compatible with a shear failure of the classical Mohr-Coulomb type in the local stress field with internal friction values between 0.6 and 1.0, contrary to what was originally understood. These values are obtained in a stress field that is mostly determined by the regional stresses, yet a modest coseismic component best predict the fracture orientation. This suggests that the crust rock is brought close to failure by quasi-static interseismic loading, and eventually breaks in the early stages of the seismic events. Our results also suggest that the regional tectonic stresses are oriented with the largest compression axis at N14E at the northern termination of the region that hosted the 2019 sequence. This orientation well captures the internal friction coefficient for the 2019 fractures that displayed horizontal slip, the damage accumulation possibly happening in quasi-static conditions, and with previous works investigating the regional tectonic stress orientation based on focal mechanisms and slip vectors.

Finally, the fractures at the northern termination that formed during the 2019 sequence show a scale separation, with short fractures characterized by dip slip and aligned with the largest compressive regional stress, and long fractures characterized by lateral motion and oriented at an angle from such stress that is consistent with commonly assumed values of internal rock friction.

ACKNOWLEDGMENTS

E.M. acknowledges funding from the Swiss National Science Foundation under grant P500PN_202863. C.C. acknowledges funding from the Southern California Earthquake Center, award 23069.

DATA AVAILABILITY

The slip models of the foreshock and mainshock by Jin & Fialko (2020) are accessible at `http://equake-rc.info/SRCMOD/searchmodels/viewmodel/s2019RIDGEC01JINx/` and `http://equake-rc.info/SRCMOD/searchmodels/viewmodel/s2019RIDGEC02JINx/`, respectively. The shapefile containing the surface ruptures identified by Ponti et al. (2020) is available at `https://doi.org/10.`

`5066/P9BZ5IJ9` (Ponti et al. 2019). The shapefile containing the Ridgecrest ruptures prior to 2019 as discussed in Thompson Jobe et al. (2020) is available at `http://dx.doi.org/10.5066/P9ENA24Y` (Philibosian et al. 2020). The results of our analyses on these datasets are available at `https://github.com/enrico-mi/Ridgecrest-visualization.git` and can be accessed interactively also at `https://www.enricomilanese.com/Ridgecrest/`. All links were last accessed at the time of submission. Maps were produced with © Mapbox and © OpenStreetMap.

REFERENCES

Anderson, E. M., 1951. *The dynamics of faulting and dyke formation with applications to Britain*, Oliver and Boyd, Edinburgh.

Antoine, S. L., Klinger, Y., Delorme, A., Wang, K., Bürgmann, R., & Gold, R. D., 2021. Diffuse deformation and surface faulting distribution from submetric image correlation along the 2019 Ridgecrest, California, ruptures, *Bulletin of the Seismological Society of America*, **111**(5), 2275–2302.

Byerlee, J., 1978. Friction of rocks, *Rock friction and earthquake prediction*, pp. 615–626.

Carpenter, B., Marone, C., & Saffer, D., 2009. Frictional behavior of materials in the 3D SAFOD volume, *Geophysical Research Letters*, **36**(5).

Cattania, C., Hainzl, S., Wang, L., Roth, F., & Enescu, B., 2014. Propagation of coulomb stress uncertainties in physics-based aftershock models, *Journal of Geophysical Research: Solid Earth*, **119**(10), 7846–7864.

Chen, K., Avouac, J.-P., Aati, S., Milliner, C., Zheng, F., & Shi, C., 2020. Cascading and pulse-like ruptures during the 2019 Ridgecrest earthquakes in the Eastern California Shear Zone, *Nature Communications*, **11**(1), 22.

Dokka, R. K. & Travis, C. J., 1990. Late Cenozoic strike-slip faulting in the Mojave Desert, California, *Tectonics*, **9**(2), 311–340.

DuRoss, C. B., Gold, R. D., Dawson, T. E., Scharer, K. M., Kendrick, K. J., Akciz, S. O., Angster, S. J., Bachhuber, J., Bacon, S., Bennett, S. E., et al., 2020. Surface displacement distributions for the July 2019 Ridgecrest, California, earthquake ruptures, *Bulletin of the Seismological Society of America*, **110**(4), 1400–1418.

Fialko, Y., 2021. Estimation of absolute stress in the hypocentral region of the 2019 Ridgecrest, California, earthquakes, *Journal of Geophysical Research: Solid Earth*, **126**(7), e2021JB022000.

Fialko, Y. & Jin, Z., 2021. Simple shear origin of the cross-faults ruptured in the 2019 Ridgecrest earthquake sequence, *Nature Geoscience*, **14**(7), 513–518.

Freund, L. B., 1998. *Dynamic fracture mechanics*, Cambridge university press.

Goldberg, D. E., Melgar, D., Sahakian, V., Thomas, A., Xu, X., Crowell, B., & Geng, J., 2020. Complex rupture of an immature fault zone: A simultaneous kinematic model of the 2019 Ridgecrest, CA earthquakes, *Geophysical Research Letters*, **47**(3), e2019GL086382.

Handin, J., 1969. On the Coulomb-Mohr failure criterion, *Journal of Geophysical Research*, **74**(22), 5343–5348.

Hardebeck, J. L. & Hauksson, E., 2001. Crustal stress field in southern California and its implications for fault mechanics, *Journal of Geophysical Research: Solid Earth*, **106**(B10), 21859–21882.

Hardebeck, J. L. & Okada, T., 2018. Temporal stress changes caused by earthquakes: A review, *Journal of Geophysical Research: Solid Earth*, **123**(2), 1350–1365.

Hauksson, E. & Jones, L. M., 2020. Seismicity, stress state, and style of faulting of the Ridgecrest-Coso region from the 1930s to 2019: Seismotectonics of an evolving plate boundary segment, *Bulletin of the Seismological Society of America*, **110**(4), 1457–1473.

Jaeger, J. C., Cook, N. G., & Zimmerman, R., 2009. *Fundamentals of rock mechanics*, John Wiley & Sons.

Jin, Z. & Fialko, Y., 2020. Finite slip models of the 2019 Ridgecrest earthquake sequence constrained by space geodetic data and aftershock locations, *Bulletin of the Seismological Society of America*, **110**(4), 1660–1679.

Lee, H. & Haimson, B. C., 2011. True triaxial strength, deformability, and brittle failure of granodiorite from the san andreas fault observatory at depth, *International Journal of Rock Mechanics and Mining Sciences*, **48**(7), 1199–1207.

Liang, C., Ampuero, J.-P., & Pino Muñoz, D., 2021. Deep ductile shear zone facilitates near-orthogonal strike-slip faulting in a thin brittle lithosphere, *Geophysical Research Letters*, **48**(2), e2020GL090744.

Liu, C., Lay, T., Brodsky, E. E., Dascher-Cousineau, K., & Xiong, X., 2019. Coseismic rupture process of the large 2019 Ridgecrest earthquakes from joint inversion of geodetic and seismological observations, *Geophysical Research Letters*, **46**(21), 11820–11829.

Milliner, C., Donnellan, A., Aati, S., Avouac, J.-P., Zinke, R., Dolan, J. F., Wang, K., & Bürgmann, R., 2021. Bookshelf kinematics and the effect of dilatation on fault zone inelastic deformation: Examples from optical image correlation measurements of the 2019 Ridgecrest earthquake sequence, *Journal of Geophysical Research: Solid Earth*, **126**(3), e2020JB020551.

Milliner, C. W. D., Aati, S., & Avouac, J.-P., 2022. Fault friction derived from fault bend influence on coseismic slip during the 2019 Ridgecrest Mw 7.1 mainshock, *Journal of Geophysical Research: Solid Earth*, **127**(11), e2022JB024519.

Morrow, C., Solum, J., Tembe, S., Lockner, D., & Wong, T.-F., 2007. Using drill cutting separates to estimate the strength of narrow shear zones at safod, *Geophysical Research Letters*, **34**(11).

Nevitt, J. M., Brooks, B. A., Hardebeck, J. L., & Aagaard, B. T., 2023. 2019 M7.1 Ridgecrest earthquake slip distribution controlled by fault geometry inherited from Independence dike swarm, *Nature Communications*, **14**(1), 1546.

Nixon, C. W., Sanderson, D. J., & Bull, J. M., 2011. Deformation within a strike-slip fault network at Westward Ho!, Devon UK: Domino vs conjugate faulting, *Journal of Structural Geology*, **33**(5), 833–843.

Okada, Y., 1985. Surface deformation due to shear and tensile faults in a half-space, *Bulletin of the Seismological Society of America*, **75**(4), 1135–1154.

Paterson, M. S. & Wong, T.-f., 2005. *Experimental rock deformation: the brittle field*, vol. 348, Springer.

Philibosian, B., Thompson Jobe, J., Chupik, C., Dawson, T., Bennett, S., Kendrick, K., DuRoss, C., Gold, R., Ladinsky, T., Haddon, E., Pierce, I., Swanson, B., & Seitz, G., 2020. Pre-existing features associated with active faulting in the vicinity of the 2019 Ridgecrest, California earthquake sequence: U.S. Geological Survey data release.

Poliakov, A. N., Dmowska, R., & Rice, J. R., 2002. Dynamic shear rupture interactions with fault bends and off-axis secondary faulting, *Journal of Geophysical Research: Solid Earth*, **107**(B11), ESE–6.

Ponti, D., Blair, J., Rosa, C., Thomas, K., Pickering, A., Morelan, A., & Dawson, T., 2019. Digital datasets documenting surface fault rupture and ground deformation features produced by the Ridgecrest M6. 4 and M7. 1 earthquake sequence of July 4 and 5, 2019: U.S. Geological Survey Data Release.

Ponti, D. J., Blair, J. L., Rosa, C. M., Thomas, K., Pickering, A. J., Akciz, S., Angster, S., Avouac, J.-P., Bachhuber, J., Bacon, S., et al., 2020. Documentation of surface fault rupture and ground-deformation features produced by the 4 and 5 July 2019 Mw 6.4 and Mw 7.1 Ridgecrest earthquake sequence, *Seismological Research Letters*, **91**(5), 2942–2959.

Renard, F., Weiss, J., Mathiesen, J., Ben-Zion, Y., Kandula, N., & Cordonnier, B., 2018. Critical evolution of damage toward system-size failure in crystalline rock, *Journal of Geophysical Research: Solid Earth*, **123**(2), 1969–1986.

Rodriguez Padilla, A. M., Oskin, M. E., Milliner, C. W. D., & Plesch, A., 2022. Accrual of widespread rock damage from the 2019 Ridgecrest earthquakes, *Nature Geoscience*, **15**(3), 222–226.

Ron, H., Beroza, G., & Nur, A., 2001. Simple model explains complex faulting, *Eos, Transactions American Geophysical Union*, **82**(10), 125–129.

Ross, Z. E., Idini, B., Jia, Z., Stephenson, O. L., Zhong, M., Wang, X., Zhan, Z., Simons, M., Fielding, E. J., Yun, S.-H., et al., 2019. Hierarchical interlocked orthogonal faulting in the 2019 Ridgecrest earthquake sequence, *Science*, **366**(6463), 346–351.

Scholz, C. H. & Choi, E., 2022. What comes first: The fault or the ductile shear zone?, *Earth and Planetary Science Letters*, **577**, 117273.

Sheng, S. & Meng, L., 2020. Stress field variation during the 2019 Ridgecrest earthquake sequence, *Geophysical Research Letters*, **47**(15), e2020GL087722.

Sibson, R. H., 1985. A note on fault reactivation, *Journal of Structural Geology*, **7**(6), 751–754.

Tembe, S., Lockner, D. A., Solum, J. G., Morrow, C. A., Wong, T.-f., & Moore, D. E., 2006. Frictional strength of cuttings and core from SAFOD drillhole phases 1 and 2, *Geophysical Research Letters*, **33**(23).

Thatcher, W. & Hill, D. P., 1991. Fault orientations in extensional and conjugate strike-slip environments and their implications, *Geology*, **19**(11), 1116–1120.

Thompson Jobe, J. A., Philibosian, B., Chupik, C., Dawson, T., Bennett, S. E., Gold, R., DuRoss, C., Ladinsky, T., Kendrick, K., Haddon, E., et al., 2020. Evidence of previous faulting along the 2019 Ridgecrest, California, earthquake ruptures, *Bulletin of the Seismological Society of America*, **110**(4), 1427–1456.

Townend, J. & Zoback, M., 2004. Regional tectonic stress near the San Andreas fault in central and southern California, *Geophysical Research Letters*, **31**(15).

Wang, K., Dreger, D. S., Tinti, E., Bürgmann, R., & Taira, T., 2020. Rupture process of the 2019 Ridgecrest, California Mw 6.4 foreshock and Mw 7.1 earthquake constrained by seismic and geodetic data, *Bulletin of the Seismological Society of America*, **110**(4), 1603–1626.

Wang, X. & Zhan, Z., 2020. Seismotectonics and fault geometries of the 2019 Ridgecrest sequence: Insight from aftershock moment tensor catalog using 3-D Green's functions, *Journal of Geophysical Research: Solid Earth*, **125**(5), e2020JB019577.

Xu, X., Sandwell, D. T., & Smith-Konter, B., 2020a. Coseismic displacements and surface fractures from Sentinel-1 InSAR: 2019 Ridgecrest earthquakes, *Seismological Research Letters*, **91**(4), 1979–1985.

Xu, X., Sandwell, D. T., Ward, L. A., Milliner, C. W. D., Smith-Konter, B. R., Fang, P., & Bock, Y., 2020b. Surface deformation associated with fractures near the 2019 Ridgecrest earthquake sequence, *Science*, **370**(6516), 605–608.

Yang, J., Zhu, H., & Lumley, D., 2020. Time-lapse imaging of coseismic ruptures for the 2019 Ridgecrest earthquakes using multiazimuth backprojection with regional seismic data and a 3-D crustal velocity model, *Geophysical Research Letters*, **47**(9), e2020GL087181.

Yang, W. & Hauksson, E., 2013. The tectonic crustal stress field and style of faulting along the Pacific North America Plate boundary in Southern California, *Geophysical Journal International*, **194**(1), 100–117.

Zoback, M. L., Thompson, G., & Anderson, R., 1981. Cainozoic evolution of the state of stress and style of tectonism of the Basin and Range province of the western United States, *Philosophical Transactions of the Royal Society of London. Series A, Mathematical and Physical Sciences*, **300**(1454), 407–434.

Supplementary Information

Supplementary Text

Stress estimates.

The stress tensor σ_{ij} at a given point is assumed as $\sigma_{ij} = \sigma_{\mathrm{reg},ij} + \sigma_{\mathrm{cos},ij}$, where $\sigma_{\mathrm{reg},ij}$ and $\sigma_{\mathrm{cos},ij}$ are the regional tectonic and coseismic stress states, respectively. $\sigma_{\mathrm{cos},ij}$ is determined via Okada-type solutions (Okada 1985) from the published slip model of Jin & Fialko (2020) (with 10 GPa shear modulus and 0.25 Poisson ratio) and is generally heterogeneous in space and depth. Identifying with $\sigma_{1,\mathrm{reg}}$, $\sigma_{2,\mathrm{reg}}$, and $\sigma_{3,\mathrm{reg}}$ the maximum, intermediate, and minimum normal stresses and following Fialko (2021), $\sigma_{\mathrm{reg},ij}$ is assumed such that the $\sigma_{1,\mathrm{reg}}$ and $\sigma_{3,\mathrm{reg}}$ are horizontal, that $\sigma_{2,\mathrm{reg}}$ is vertical, and that $\sigma_{1,\mathrm{reg}} = \sigma_{2,\mathrm{reg}} = 3\sigma_{3,\mathrm{reg}}$, where $\sigma_{1,\mathrm{reg}}$ is assumed to be determined by the effective lithostatic stress (Fialko 2021). The latter is $(\rho_{\mathrm{s}} - \rho_{\mathrm{w}})\, gz$, where ρ_{s} and ρ_{w} are densities of the rock and the water, g is gravity and z is depth. We assumed $\rho_{\mathrm{s}} = 2700$ kg/m^3, $\rho_{\mathrm{w}} = 1000$ kg/m^3, and $g = 9.8$ m/s^2. The largest horizontal compressive stress $\sigma_{\mathrm{H}} = \sigma_1$ and its direction at depth z are computed assuming that it lies on the horizontal plane. $\sigma_{\mathrm{reg},ij}$ being lithostatic, its magnitude increases with depth and for large z it is $\sigma_{ij} \approx \sigma_{\mathrm{reg},ij}$ and $\theta_{\mathrm{H}} = \theta_{\mathrm{H,reg}}$, which is constant with space and depth.

For the orientation $\theta_{\mathrm{H,reg}}$ of the regional stress, values between N0E and N15E are reported for the region, where the most northward values are generally suggested at the scale of the whole region and the most eastward values for the northern termination of the 2019 mainshock fault, i.e. our area of interest. In their investigations of Ridgecrest stress changes, (Xu et al. 2020b) assume NS compression based on (Townend & Zoback 2004), who compile estimates from different techniques (borehole breakouts, hydraulic fracturing experiments, focal mechanism inversions, lithospheric buoyancy and plate interaction modeling, SAFOD drillhole). In their modeling of fault and stress state rotation, (Fialko & Jin 2021) use the estimates of (Yang & Hauksson 2013) based on inversion from focal mechanisms in Southern California. Estimates of stress orientation focused on the 2019 Ridgecrest events found pre-earthquake orientations of N11E (Wang & Zhan (2020), from earthquake focal mechanisms), N10.8E± 2.8 (Sheng & Meng (2020), from earthquake focal mechanisms), and N13E (Milliner et al. (2022), from coseismic slip vectors inversion). As for the coseismic stress state, we reconstruct it by means of Okada dislocations (Okada 1985) from the slip model published by Jin & Fialko (2020). We can then think of the superposition of $\sigma_{\mathrm{reg},ij}$ and $\sigma_{\mathrm{cos},ij}$ as the stress state at the peak of slip during the M_w 7.1 mainshock.

Fractures dataset.

The fractures investigated in this work are a subset of the ruptured surfaces reported by Ponti et al. (2020) and selected as follows.

The geometry and location of the ruptures discussed by Ponti et al. (2020) is made publicly available by the authors in the form of a shapefile (Ponti et al. 2019). Each fracture is described also by several attributes – the primary observation method, their origin, the date the fracture was mapped, and others. To include in our analysis only those ruptures due to faulting, we selected fractures whose origin has been classified as tectonic by the authors (discarding ruptures attributed to lateral shaking or of uncertain origins). The dataset that is publicly available does not contain fractures classified as not verified on the field, thus they are not considered in our analysis. This is the set represented with orange lines in Fig. 1a.

While Ponti et al. (2020) report that the observed surface ruptures have originated during the 2019 Ridgecrest sequence, later Thompson Jobe et al. (2020) discuss evidence that a consistent subset of those pre-dated such sequence. The geometry and location of the neotectonic features discussed by Thompson Jobe et al. (2020) is also publicly available in the form of a shapefile with several attributes. We thus considered those fractures classified as geologic or with no specific classification, i.e. we did not consider fractures classified as due to artificial origins or of uncertain date ('subtle'). We then compared this dataset with the one of reference described above, and removed from the latter all those fractures whose geometrical center is within a 30 m radius of the geometrical center of any of the fracture segments in the subset from Thompson Jobe et al. (2020). The final subset thus contains the best guess of coseismic surface ruptures available in the literature, and it is characterized by the lengths ands strikes in Supplementary Figs S1 and S10, respectively. This is the subset of reference throughout the manuscript, if not otherwise stated.

Each shapefile contains a series of surface ruptures whose geometry is described by linked straight segments. All our analyses investigate the orientation and lengths of the segments, and for the sake of simplicity throughout the manuscript and supplementary information we use the terms 'fracture' and 'segment' interchangeably.

As we are particularly interested in the fractures that form a high angle with the main fault and whose orientation has been described as mechanically unfavourable (Ross et al. 2019; Milliner et al. 2021), we focus on the region at the northern termination of the main fault selecting only the fractures fully contained in the region of longitude $[-117.74, -117.63]$ and latitude $[35.82, 35.94]$.

Information on the dominant slip sense for each fractures is inferred from the works of DuRoss et al. (2020); Xu et al. (2020a); Antoine et al. (2021), and the same slip sense is assigned to all the segments of each fracture. When conflicting information is reported, we select the most reported sense.

(Xu et al. 2020a), for example, identify the fractures of our interest almost exclusively as left-lateral (fig. 4 of their manuscript), and do not distinguish any vertical motion in the whole Ridgecrest region. While this is accurate as a first order behavior, finer analyses by (DuRoss et al. 2020; Antoine et al. 2021; Milliner et al. 2021) allowed us to more accurately identify the faults actually displaying right-lateral and dip slip motion.

As different fractures can have widely different resolutions, e.g. depending on the method of observation, we performed analysis at different scales homogeneising smaller scales details. This is achieved as follows. For a given lengthscale L and each fracture i, we first compute the integer number of segments in which to rediscretize the fracture as $n_{\text{new},i} = \lfloor l_i/L \rfloor$, where l_i is measured as the distance between the first and last point of the fracture (not as the sum of all the fracture segments' lengths) and $\lfloor \cdot \rfloor$ is the floor function. We then remove from the dataset all those fractures for which $n_{\text{new},i} < 0$, and keep as are those for which $n_{\text{new},i} = 1$. We then rediscretize those with $n_{\text{new},i} > 1$ by drawing a straight reference line between the ending points of the fracture, subdividing it in $n_{\text{new},i}$ segments with $n_{\text{new},i} - 1$ equally spaced intermediate points I_j , and finding each point P_j that belongs to the original segments and whose projection meets the reference line at I_j. The segments linking the original end points of the fracture through the points P_j now constitutes the fracture i resolved at the lengthscale L. The procedure is illustrated in Supplementary Fig. S11.

Angles and error estimation.

All angles are estimated at the center of each fracture segment, for both the fractures derived from Ponti et al. (2020) dataset and the estimation from the static stress analysis.

For a given coefficient μ and stress state, we measure the misfit by computing the sum of residuals $\text{SR}_\text{w} = \sum_s \epsilon_{\text{w},s}$, where the sum is over all the segments and ϵ_w is the weighted error computed as follows. Identifying the s-th segment by its orientation θ_s, and considering the orientation $\theta_{\text{H},s}$ of the largest local horizontal stress $\sigma_{\text{H},s}$ (measured at the center of the segment s), and the rock coefficient of friction μ, the absolute error is estimated as

$$\epsilon_\text{abs}\left(\theta_s, \theta_{\text{H},s}, \mu\right) = \min|\theta_s - (\theta_{\text{H},s} \pm \theta_\mu)| \quad , \tag{1}$$

where $\theta_\mu = \left(\pi/2 - \tan^{-1}\mu\right)/2$ and the positive (negative) sign indicates the right-lateral (left-lateral) failure plane, assuming positive angles if measured counter-clockwise. As fractures in the dataset have different resolutions depending, e.g., on the method of observation, the weighted error takes into account this by scaling the absolute error by the segment length l_s,

$$\epsilon_\text{w}\left(\theta_s, \theta_{\text{H},s}, \mu, l_s\right) = \epsilon_\text{abs}\left(\theta_s, \theta_{\text{H},s}, \mu\right) \cdot \frac{l_s}{l_\text{tot}} \quad , \tag{2}$$

where $l_{\text{tot}} = \sum_s l_{\text{s}}$ is the sum of the length of all the segments in the considered dataset.

When we investigate fractures of unknown slip sense, the value of ϵ_{abs} does not contain information on the failure direction (right-lateral or left-lateral). The maximum value ϵ_{max} of the absolute error depends on μ,

$$\epsilon_{\text{max}}\left(\mu\right) = \pi/2 - \theta_\mu \quad . \tag{3}$$

as $\theta_s \in (-\pi/2, \pi/2]$ and both positive and negative θ_μ are considered. The maximum error is then minimum for $\mu = 0$, $\epsilon_{\text{max}}\left(\mu = 0\right) = \pi/4$, and maximum for $\mu \to \infty$, $\epsilon_{\text{max}}\left(\mu \to \infty\right) = \pi/2$. To compare errors estimated from different values of μ, the absolute error is then normalized by its maximum value, and we call this quantity relative error ϵ_{rel}:

$$\epsilon_{\text{rel}}\left(\theta_s, \theta_{\text{H},s}, \mu\right) = \frac{\epsilon_{\text{abs}}\left(\theta_s, \theta_{\text{H},s}, \mu\right)}{\epsilon_{\text{max}}\left(\mu\right)} \quad . \tag{4}$$

In Eq. 2 we then replace ϵ_{abs} with ϵ_{rel} when we do not take into account of the slip mechanism.

Heatmaps

We summarize our results in discrete heatmaps (e.g. Supplementary Figs S3 and S12), where each tile's color is directly proportional to the sum of squared residuals of the weighted error of the predicted orientation of each fracture, $\text{SR}_{\epsilon_\text{w}}$, and where each row and column represents a value of μ and of depth. At each depth, orange borders surround neighboring tiles whose $\text{SR}_{\epsilon_\text{w}}$ is smaller than the one predicted by pure randomness, and an orange ring identifies the tile with the smallest $\text{SR}_{\epsilon_\text{w}}$. For each heatmap, an orange filled circle identifies the tile with the smallest $\text{SR}_{\epsilon_\text{w}}$ overall. An interactive version of the heatmaps where the user can explore the dataset is available at `https://www.enricomilanese.com/Ridgecrest` (and it can be downloaded at `https://github.com/enrico-mi/Ridgecrest-visualization.git`), and it includes further visualizations, namely a map of the region that shows the selected fractures, the orientations of stress lines (tensile and sinistral and dextral shear), and a polar distribution of the visualized fractures.

4.1 Supplementary Figures

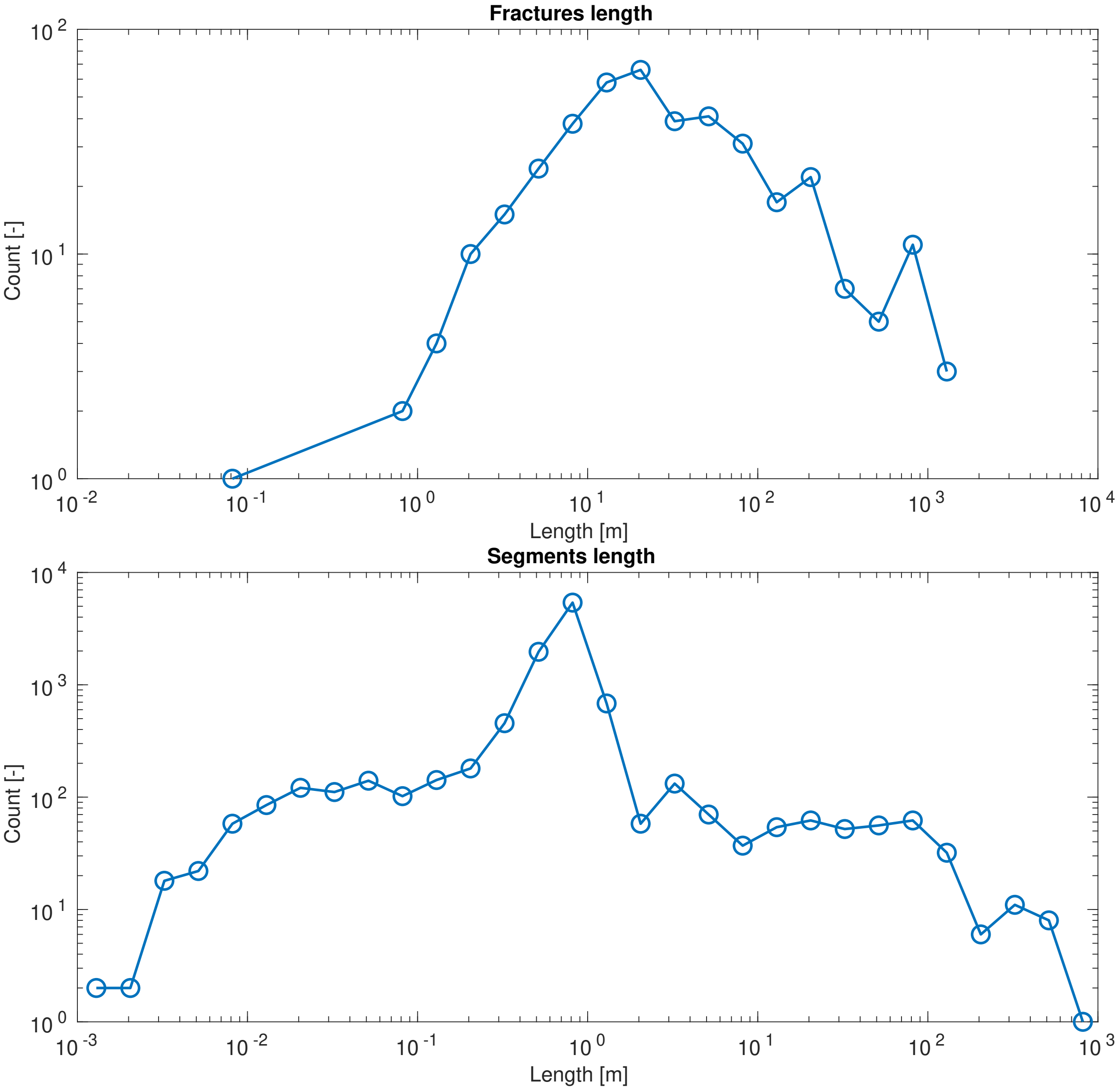

Figure S1. Distribution of the lengths of the fractures (top) and their segments (bottom) of the dataset subset from (Ponti et al. 2020) analyzed in this work (yellow fractures within the dashed box of Fig. 1a. When not otherwise specified, our analyses investigate the orientation and lengths of the segments.

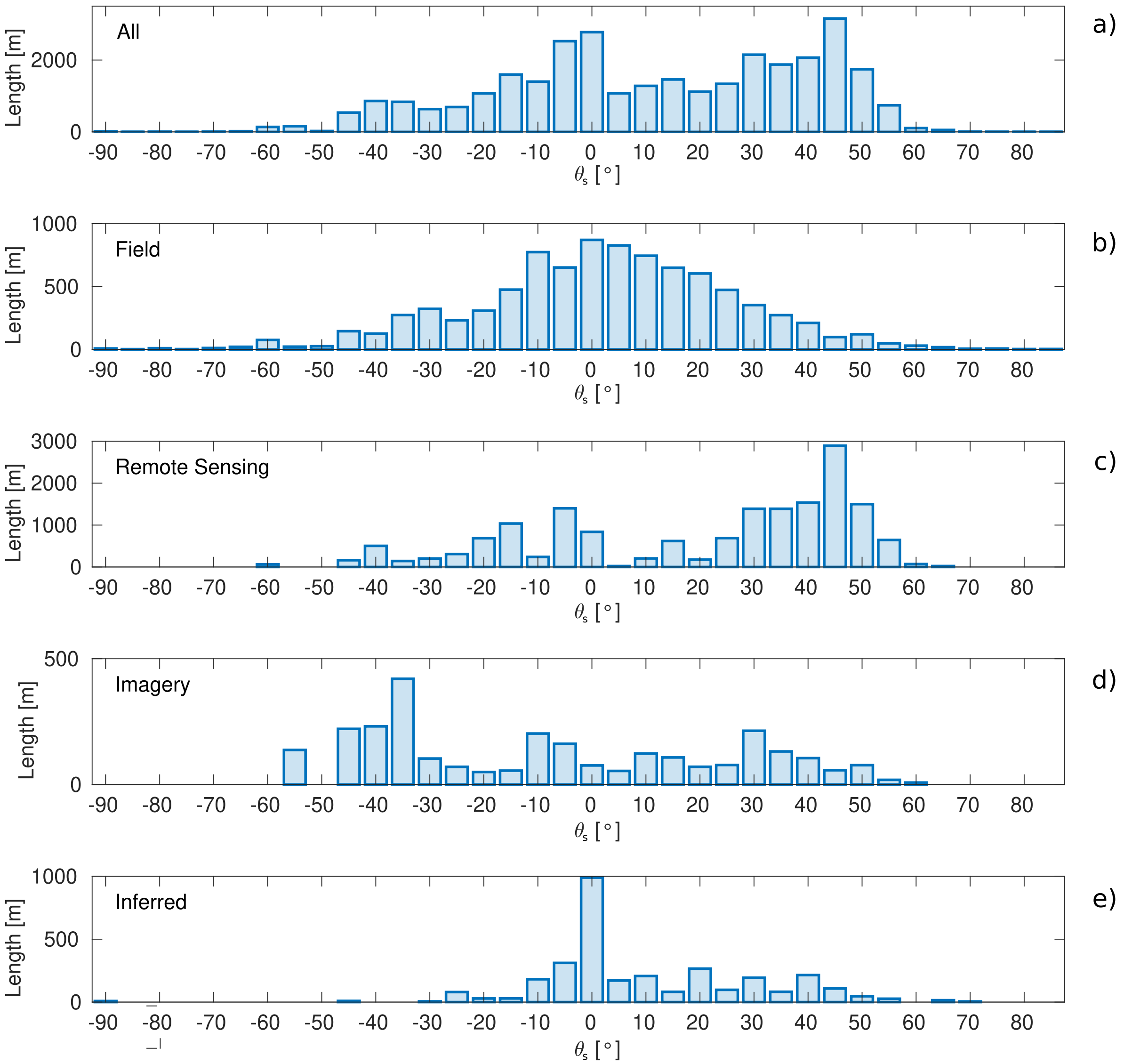

Figure S2. Dependence of fractures strikes on observation methodology. Fractures observed on the field (b) and with remote sensing (c) constitute most of all the ruptured surfaces (a), making up for 28% and 53% of the total length, respectively. The two subsets display different orientations: 'field' fractures are clustered around N0E, 'remote sensing' fractures show a bimodal distribution with a peak at N45E and second peak at N5W. Fractures detected with imagery (c) and inferred (d) constitute 9% and 10% of the total length, respectively.

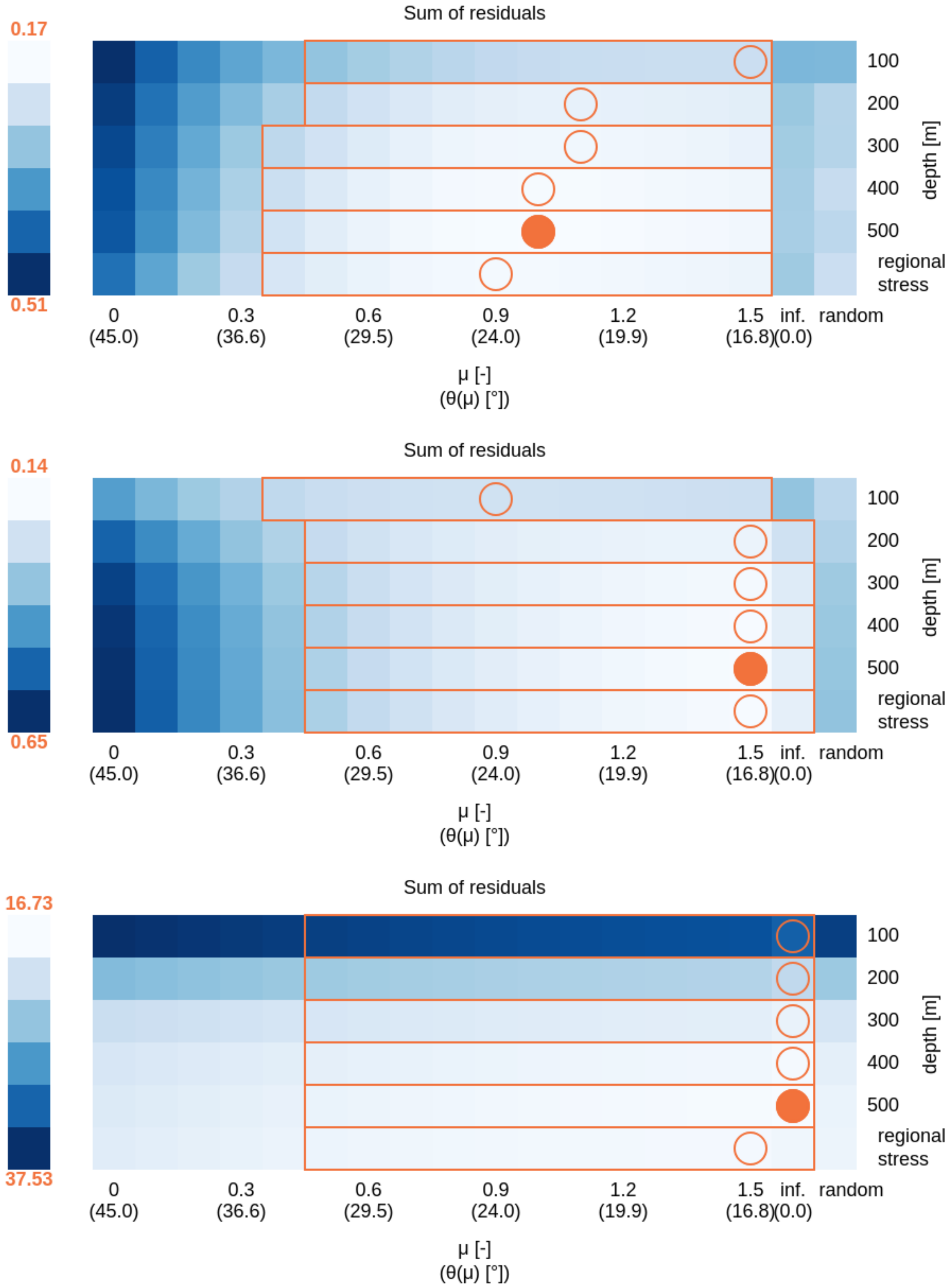

Figure S3. Lengthscale effects on sum of residuals $\mathrm{SR_w}$, $\theta_{\mathrm{H,reg}}$ at N14E, $k = 1$, at 100 m to 500 m depth. a) and b) consider all the fractures, independent of the their slip sense, split in fractures shorter and longer than 10 m, respectively. With respect to the case where the fractures length is not considered (Supplementary Fig. S12), shorter (longer) fractures show best fits for larger (smaller) values of μ, suggesting different failure mechanisms at different scales. c) Best fit for fractures of known slip mechanism, shorter than 10 m. The best

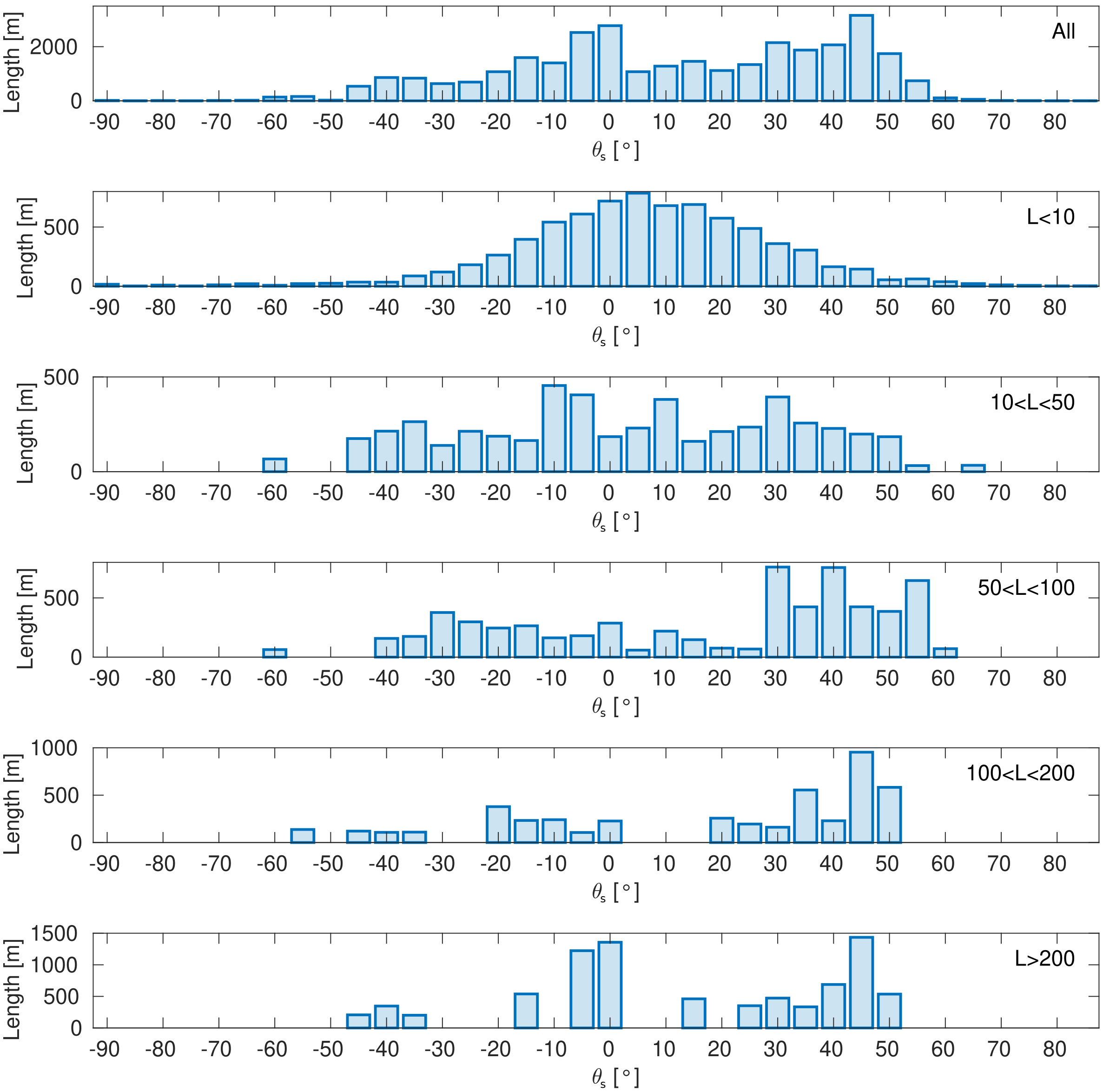

Figure S4. Dependence of fractures strikes on their length L. The whole set (a) has two peaks at N45E and N0E, consistently with the best fit for $\mu = 1.2$ ($2\theta = 40°$). Fractures shorter than 10 m cluster around N5E (b), fractures between 10 m and 50 m show a larger spread (c), with peaks at N10W, N10E, and N30E, and longer fractures show strong peaks at between N30E and N55E (d-f) (and at N0E for $L > 200$m, (f)).

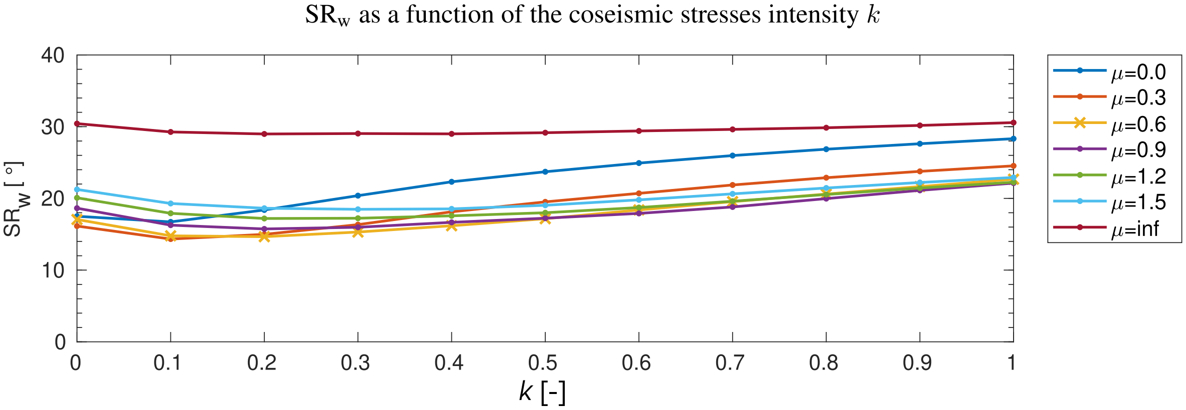

Figure S5. Sum of residuals SR$_\mathrm{w}$ as a function of the of the coseismic stresses intensity k, for $\theta_\mathrm{H,reg}$ at N0E. Solid colored lines identify select values of μ. SR$_\mathrm{w}$ is computed from the total stresses at 100 m depth, regional stresses oriented at N0E. SR$_\mathrm{w}$ is minimum for $k = 0.1$ and $\mu = 0.3$.

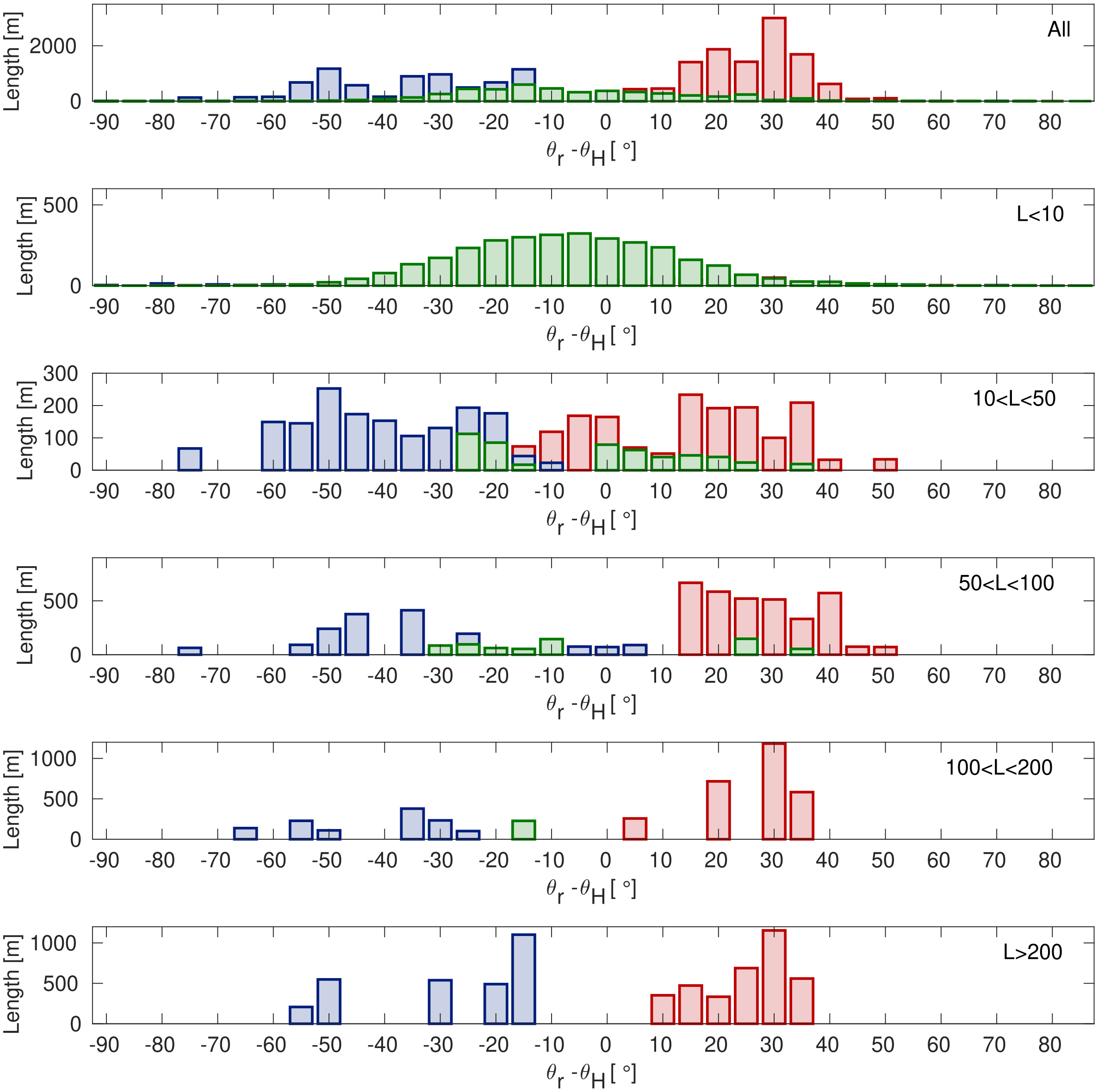

Figure S6. Distribution of $\theta_s - \theta_H$ at different lengthscales for fractures of known slip sense, $\theta_{H,reg}$ at N14E, and no coseismic stresses. From top to bottom, we consider all the fractures, fractures shorter than 10 m, between 10 and 50 m long, between 50 and 100 m long, between 100 and 200 m long, and longer than 200 m. The predominant motion of short fractures ($L < 10$ m) is dip slip, while fractures longer than 10 m host horizontal displacement. Short fractures ($L < 10$ m) cluster around $\theta_s - \theta_H = -5°$. Dextral fractures distribution shows largest peaks at $[-55°, -30°]$, sinistral for $[15°, 35°]$, suggesting a dihedral angle $2\theta_H = 65 - 70°$ (thus $\mu \approx 0.4$). Angles are positive if clockwise, thus expected slip sense is sinistral (dextral) when $\theta_s - \theta_H$ is positive (negative).

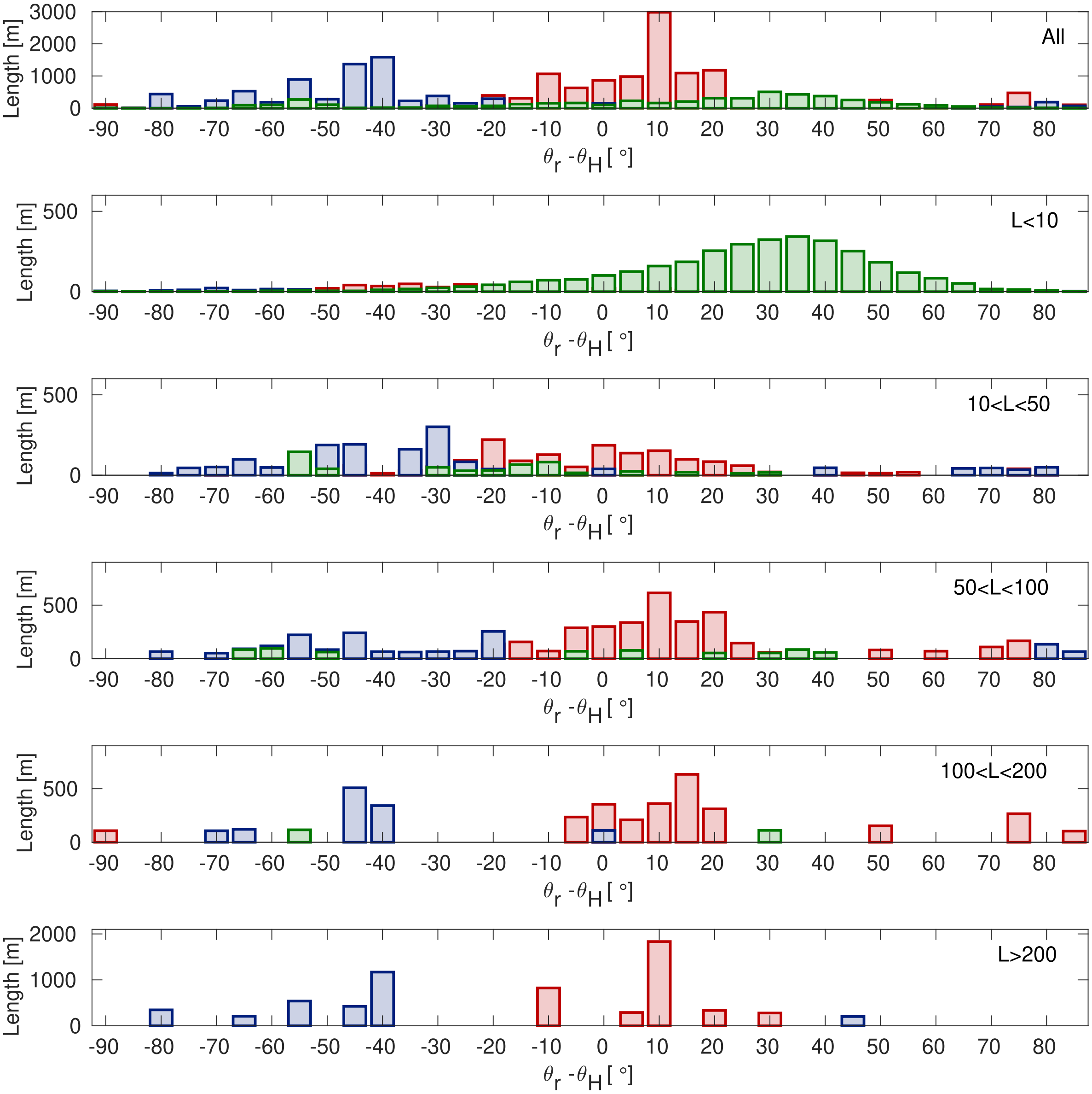

Figure S7. Distribution of $\theta_\mathrm{s} - \theta_\mathrm{H}$ at different lengthscales for fractures of known slip sense, $\theta_\mathrm{H,reg}$ at N14E, coseismic and regional stresses at 100 m deoth. From top to bottom, we consider all the fractures, fractures shorter than 10 m, between 10 and 50 m long, between 50 and 100 m long, between 100 and 200 m long, and longer than 200 m. The predominant motion of short fractures ($L < 10$ m) is dip slip, while fractures longer than 10 m host horizontal displacement. Short fractures showing dip slip (green, $L < 10$ m) cluster around $\theta_\mathrm{s} - \theta_\mathrm{H} = 35°$, suggesting that this stress configuration does not well capture fractures mechanical origins. Similarly, dextral fractures distribution (blue) shows largest peaks for $\theta_\mathrm{s} - \theta_\mathrm{H} = -40°$, sinistral (red) for $\theta_\mathrm{s} - \theta_\mathrm{H} = 10°$, suggesting a dihedral angle $2\theta_\mathrm{H} = 50°$ (thus $\mu \approx 0.9$), but the two sets are not symmetrical with respect $\theta_\mathrm{s} - \theta_\mathrm{H} = 0°$ to as it would be expected. Angles are positive if clockwise, thus expected slip sense is sinistral (dextral) when $\theta_\mathrm{s} - \theta_\mathrm{H}$ is positive (negative).

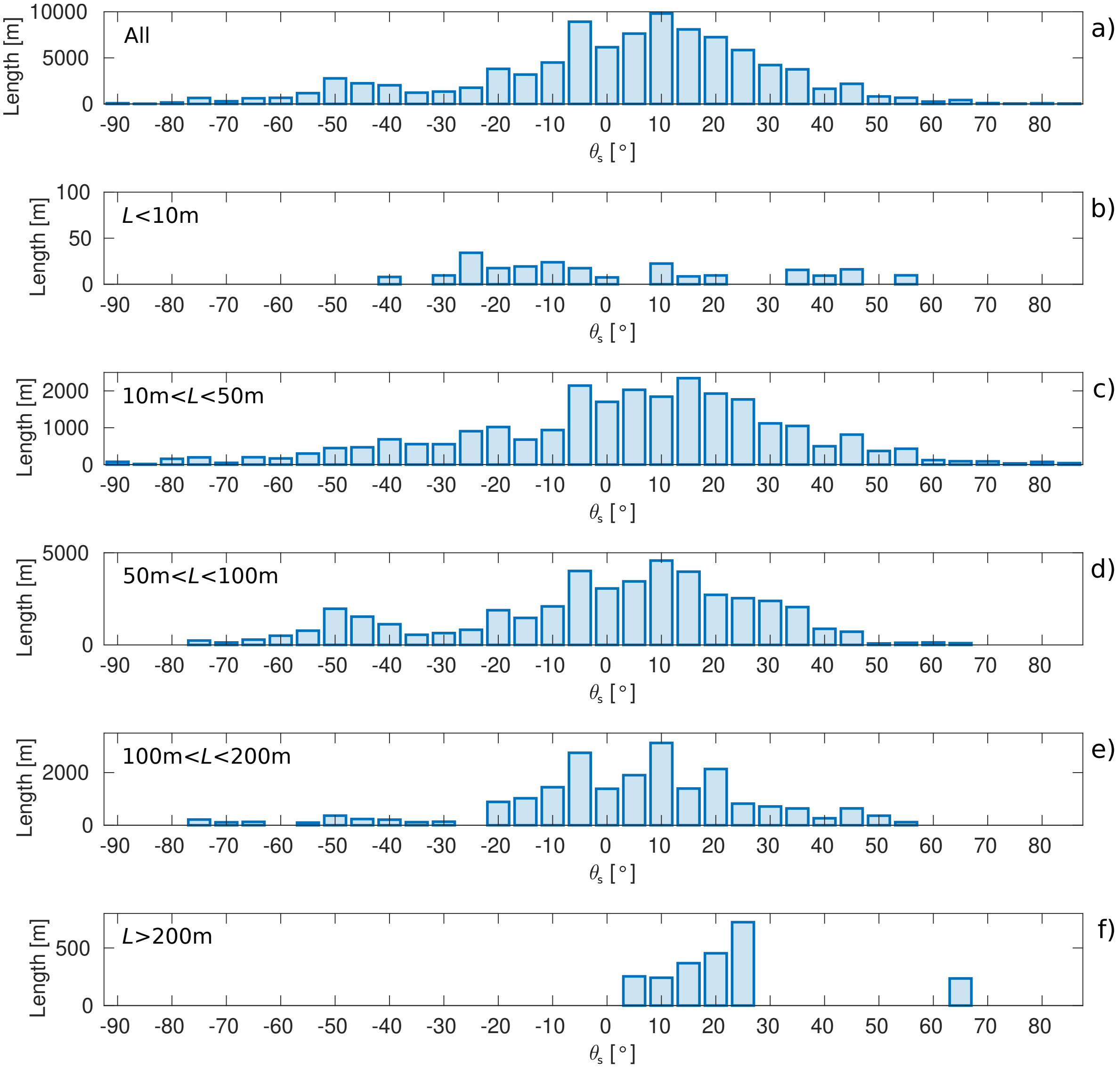

Figure S8. Distribution of strikes at different lengthscales for fractures antecedent 2019 in the considered area (dark grey lines in Fig. 1b). From top to bottom, we consider all the fractures, fractures shorter than 10 m, between 10 and 50 m long, between 50 and 100 m long, between 100 and 200 m long, and longer than 200 m. The largest peak is at N10E, and a second peak is present at N50W. Angles are positive if clockwise, thus positive (negative) values indicate strike oriented east (west) of north.

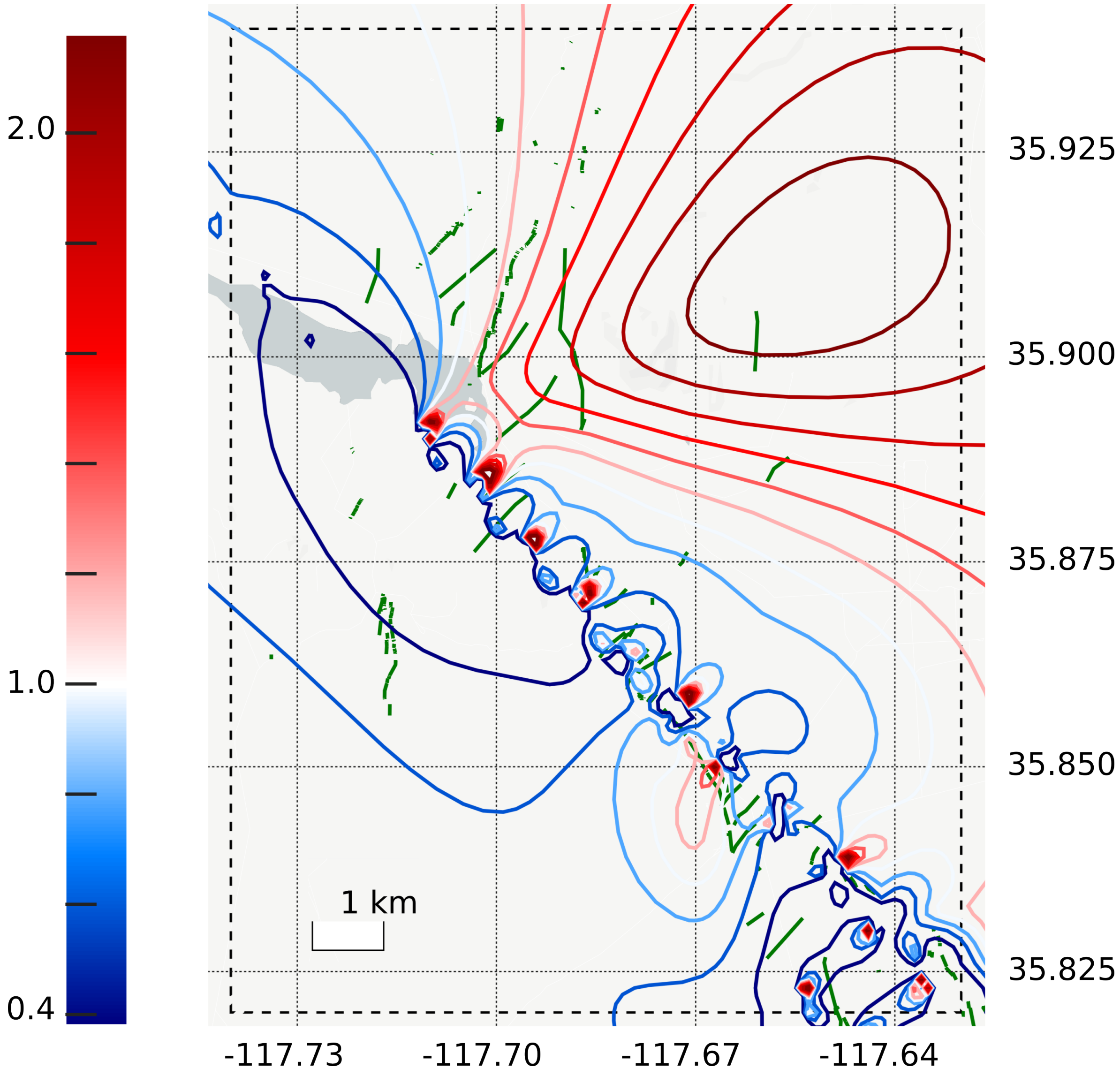

Figure S9. Coseismic faulting mode in the studied area. Blue-to-red isolines show values of $\sigma_\mathrm{v}/\sigma_\mathrm{H}$ for stresses computed at 100 m depth, θ_H at N14E. Values larger (smaller) than unity indicate regions of expected normal (strike-slip) faulting. For clarity, coseismic fractures are here reported in dark green, and features antecedent 2019 are not displayed. The region East of the fault favours normal faulting, consistently with the area being in the extensional quadrant (the main fault slipped right-laterally) and regional tectonic stresses $\sigma_\mathrm{v,reg} = \sigma_\mathrm{H,reg} = 3\sigma_\mathrm{H,reg}$ (see Supplementary Text).

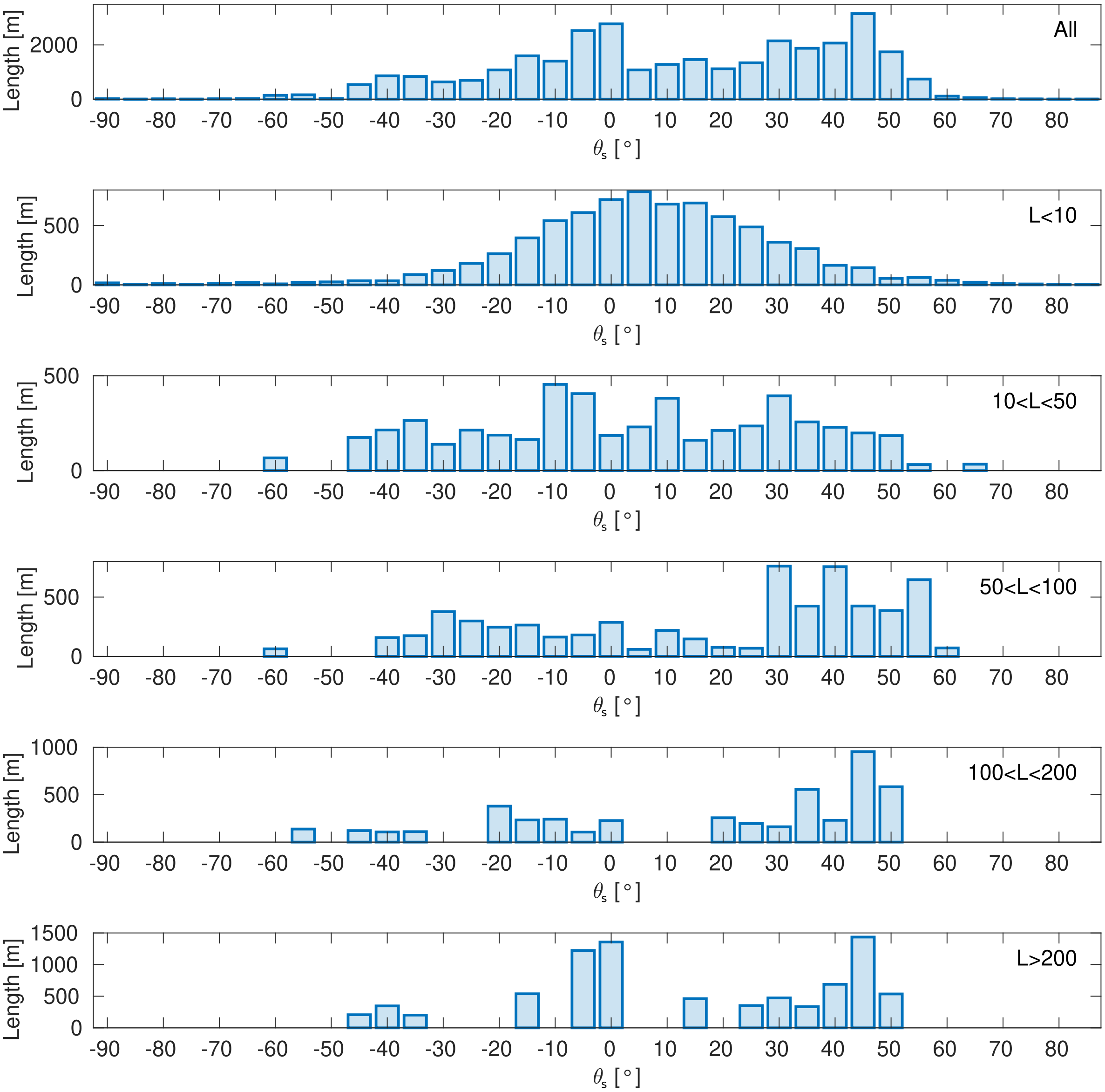

Figure S10. Distribution of $\theta_{\mathrm{s}} - \theta_{\mathrm{H}}$ at different lengthscales for all fractures, $\theta_{\mathrm{H,reg}}$ at N0E, and no coseismic stresses. As $\theta_{\mathrm{H,reg}}$ is at N0E and only regional stress is considered, this is equivalent to the strike distribution. From top to bottom, we consider all the fractures, fractures shorter than 10 m, between 10 and 50 m long, between 50 and 100 m long, between 100 and 200 m long, and longer than 200 m. Short fractures ($L < 10$ m) cluster around $\theta_{\mathrm{s}} - \theta_{\mathrm{H}} = 5°$. Longer fractures dominate the overall distribution with peaks at $0°$ and $45°$. Angles are positive if clockwise, thus expected slip sense is sinistral (dextral) when $\theta_{\mathrm{s}} - \theta_{\mathrm{H}}$ is positive (negative).

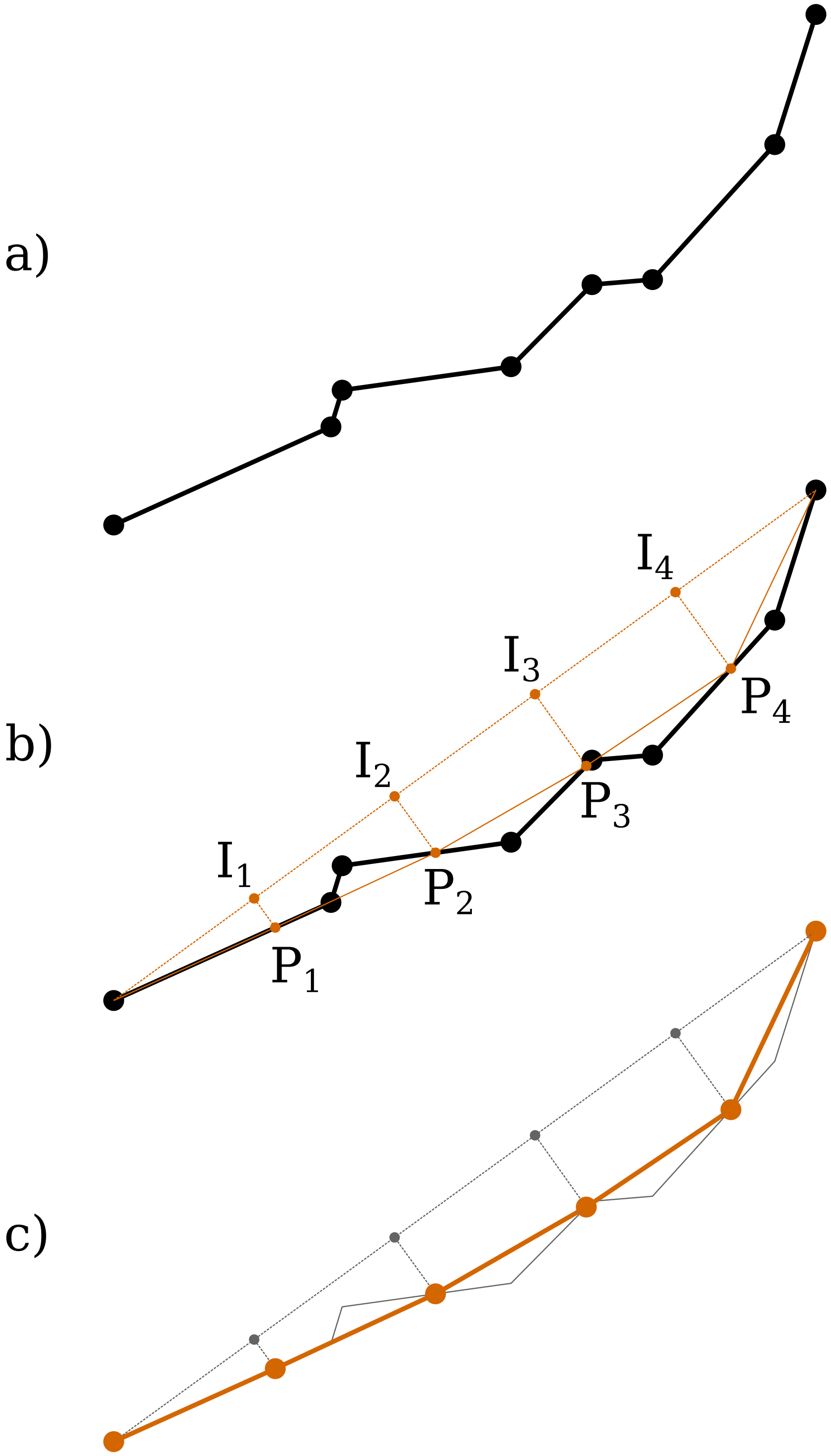

Figure S11. Procedure performed to resolve fractures in an homogeneous fashion for a prescribed resolution length L. The original fracture (a) is in this example discretized at an arbitrary length L that is a fifth of the distance between the fracture's endpoints. b) The construction line between its endpoints (dotted orange) is evenly split in five segments with new intermediate points I_j, from where the P_j points in the original fracture's segments are found. c) The new fracture (solid, orange) is made of the original endpoints and the new P_j points. Original fracture in solid gray line and construction lines in dotted gray lines.

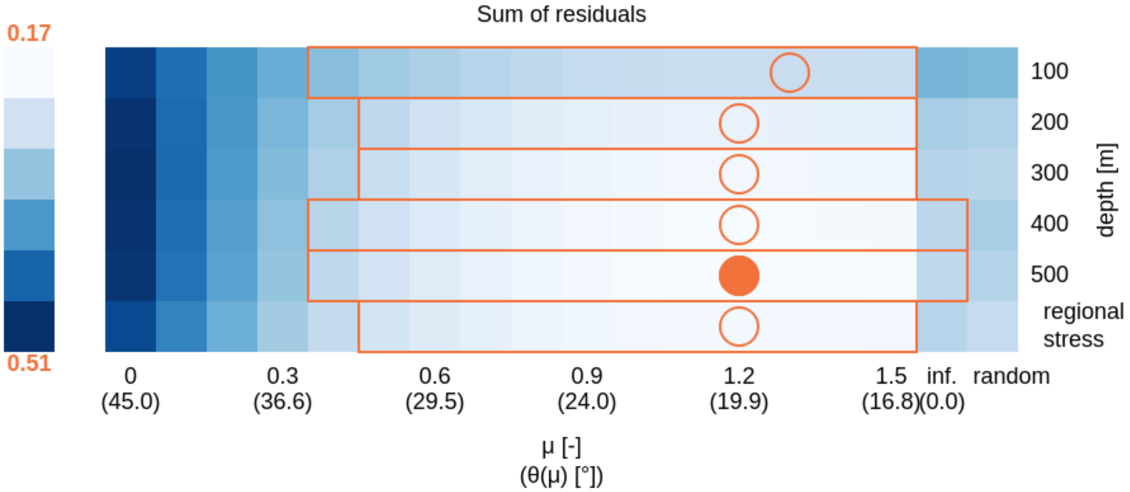

Figure S12. Sum of residuals $\mathrm{SR_w}$ for all the fractures considered, $\theta_{\mathrm{H,reg}}$ at N14E, $k = 1$, at 100 to 500 m depth. Orange solid circle indicates the combination of depth and μ that gives the lowest residual overall; empty circle indicates μ value that gives lowest residual at each depth; orange rectangle indicates, for each depth, the range of μ values that give lower values than randomness (last column); 'inf.' indicates $\mu \to \infty$ ($\theta_\mu = 0$). Best fit is for $\mu = 1.2$ at 500 m depth, where coseismic stresses are relatively less important than regional stresses. Interactive version available at `https://github.com/enrico-mi/Ridgecrest-visualization.git`.